nature materials

Article

https://doi.org/10.1038/s41563-026-02532-7

An iontronic reservoir for highly robust neuromorphic prosthesis

Received: 19 February 2025

Accepted: 5 February 2026

Published online: 09 March 2026

Check for updates

Mengjiao Pei[1,8], Tian Gao[2,8], Li Liu[3,8], Wenlong Li[4,5], Haotian Long[1], Yifei Luo[4,5], Zhaogang Teng[6], Hangyuan Cui[1], Xiang Li[1], Qinyong Dai[1], Kailu Shi[1], Lesheng Qiao[1], Baocheng Peng[1], Qianye Xing[1], Manhua Wen[1], Mengtao Han[1], Zhenhua Wan[1], Yun Li[1] ✉, Bin Xue[2] ✉, Yi Cao[2], Yi Shi[1] ✉, Qing Wan[7] ✉, Xiaodong Chen[4,5] ✉ & Changjin Wan[1,7] ✉

Neuromorphic prosthesis demands not only the assembly of neural architectures and functions but also robustness against unpredictable failures in dynamic physiological environments. While self-healing electronics have been demonstrated to restore synapse-like functions, their application to higher-order cognitive functions remains limited. Here we present a hydrogel-based iontronic reservoir that demonstrates exceptional physical and functional robustness for neuromorphic prosthesis. The nonlinear dynamics of the hydrogel–electrode interface can serve as a physical reservoir to preprocess time series, with minimized susceptibility to physical damage. Our system based on the hydrogel-based iontronic reservoir achieves 95% accuracy in speech recognition and can restore such capability within 0.02 s after reattaching the fractured points, outperforming biological systems in the neurorehabilitation process. Moreover, its pH-sensitive dynamics enable adaptive closed-loop neural stimulation control in a rat model, validating its potential for neural rehabilitation and sensorimotor function restoration. We expect such a hydrogel-based iontronic reservoir to improve both processing efficiency and robustness for next-generation neuroprosthetics and human–machine interfaces.

Neuromorphic engineering has evolved from merely mimicking neural architectures to actively interfacing with biological tissues, giving rise to the emerging field of neuromorphic bio-hybrid systems[1–5]. This paradigm shift has leveraged neuro-inspired computation for neuroprosthetics[6–9]. Recent developments in artificial neurons for neuro-substitution have shown great potential for restoration of sensor or motor functions by integrating neuromorphic elements[10–12]. For example, a chemically mediated artificial neuron demonstrates adaptive dopamine-mediated interaction with live neurons and peripheral nerves, where an electrochemical sensor regulates a memristor with synaptic plasticity to control neurotransmitter release from hydrogels[13]. However, translating such advancements into practical neuromorphic prostheses remains a challenge. This requires not only tailoring material dynamics to emulate neuronal behaviours for intelligent tasks like classification and prediction, but also adaptively tuning dynamics in response to fluctuating biological signals. Furthermore, to enable a practicable substitution of nervous tissue, physical and functional robustness against unpredictable injuries or malfunctions is as critical as functional replacement.

Recent advancements in self-healing materials have demonstrated remarkable recovery capabilities in functions such as sensing, Boolean logic and even neuron-like behaviors[14,15]. For instance,

A full list of affiliations appears at the end of the paper. ✉e-mail: yli@nju.edu.cn; xuebinnju@nju.edu.cn; yshi@nju.edu.cn; wanqing@nju.edu.cn; chenxd@ntu.edu.sg; cjwan@nju.edu.cn

self-healing supramolecular polymers have enabled the restoration of NAND, NOR and inverter functions in electronic components after damage[16]. Similarly, self-healing ionic gels, such as poly(vinylidene fluoride-co-hexafluoropropylene) P(VDF-HFP)/1-ethyl-3-methylimidazolium bis(trifluoromethylsulfonyl)imide (EMITFSI), have been employed to develop memtransistors that mimic synaptic adjustments after structural disruption[17]. While these pioneering works have demonstrated synaptic recovery via self-healing gels, they have not addressed the cognitive-level restoration required for sophisticated intelligent tasks. Moreover, in conventional neuromorphic systems, the disruption of devices typically necessitates extensive algorithmic retraining to resume normal operation, thereby undermining system reliability. Therefore, a critical need exists for robust neuromorphic devices capable of instantaneous recovery from physical damage while reliably handling adaptive signal preprocessing even in the presence of environmental noise.

Here we present a hydrogel-based iontronic reservoir (HIRE) that leverages nonlinear interfacial dynamics to enable high robustness, adaptability and closed-loop neural stimulation control for a neuromorphic prosthesis. As the ion dynamics are confined to the nanoscale iontronic interface, the HIRE is inherently robust against mechanical disruptions and enables training-free functional recovery following damage, outperforming previous physical reservoirs based on bulk dynamics. The device is fabricated with the structure of a three-terminal planar memcapacitor, incorporating a self-healing hydrogel (SHH) composed of physically crosslinked polyethyleneimine (PEI) and polyacrylic acid (PAA; crosslinked, PAA/PEI) as the dielectric layer and laser-induced graphene (LIG) as electrodes. Simulations on nine benchmark tasks demonstrate computational accuracies exceeding 90%, while hardware tests show immediate restoration of preprocessing capabilities within 0.02 s after reattaching the fracture surfaces. Remarkably, the HIRE can be functionally integrated as a neuromorphic prosthesis, where its pH-sensitive dynamics enable adaptive voice command recognition for closed-loop neural stimulation control, validating its potential for applications such as sensorimotor function restoration. By combining high efficiency of preprocessing, physical and functional robustness and biocompatibility, our HIRE represents an important advancement for next-generation neuroprosthetics, brain–machine interfaces and bio-hybrid intelligent systems.

Structural and self-healing properties of the hydrogel reservoir

The electrical double layer (EDL) is a fundamental concept in electrochemistry, describing the structure formed at the interface between a conductive electrode and an electrolyte[18]. The total thickness of the EDL is typically on the nanometre scale (with a thickness of δ), ranging from a few nanometres to tens of nanometres, depending on factors such as ion concentration and temperature[19,20]. This thickness is significantly lower than that of the bulk materials (with a thickness of d, $\delta \ll d$), which underlies the abnormally large specific capacitance ($\geq$1 μF cm^{-2}). The temporal dynamics of the EDL always have a nonlinear and fading-memory manner, matching well with the essentials for reservoir computing (RC)[21,22]. Additionally, such dynamics are confined to nanometre-scale stern and diffuse layers at electrolyte–electrode interfaces, which theoretically minimizes susceptibility to physical deformation (for example, stretching and compressing), and it's possible to retain such dynamics after a cut-and-heal process of self-healing materials. Herein we propose a HIRE for robust, restorable preprocessing in mechanically demanding environments (Fig. 1a). Such a HIRE would enhance the computational capabilities of neuro-substitutions, as RC has been demonstrated with efficient processing capabilities on multimodal time-series signals (Fig. 1b).

The hardware implementation comprises an Arduino connected to the HIRE device through test leads and a digital-to-analog converter (DAC) module. Input (IN), output (OUT) and ground (GND) channels are blue, red and green leads, respectively. The communication between the device and microprocessor is achieved by the DAC module (Fig. 1c). The SHH was fabricated using a non-covalent bonding approach through electrostatic interactions within PEI and PAA crosslinked networks (Supplementary Fig. 1; Methods for details). Such a HIRE device shows mechanical robustness under six distinct physical states, as shown in Fig. 1d. Gradual crack disappearance over time was characterized by optical microscopy during the healing process (Fig. 1e). Polymer chain migration across interfaces is clearly shown by confocal microscopy using PAA chains labelled with fluorescein *o*-acrylate. Interpenetration and entanglement were realized between the two fractured parts. Quantitative analysis of fluorescence intensity migration (Supplementary Fig. 2) confirms that healing occurs through interdiffusion and re-entanglement of PAA and PEI polymer chains over time. In cutting–healing experiments, the hydrogel restored 77.8 ± 2.8% of its initial strain endurance after ~9 min of healing at room temperature (Fig. 1f). Once the fractured surfaces are brought into contact, they exhibit immediate adhesive properties and do not spontaneously separate when one side of the crack is dragged (Supplementary Video 1). To specifically assess the recovery of interfacial adhesion, T-peel tests were conducted (Fig. 1g). Both the maximum peel force (F_{max}) and the calculated peel strength (F_{max}/W, where W is the specimen width in mm) progressively increased with longer healing times, approaching the values of a partially cut, intact control sample (Supplementary Fig. 3). The self-healing mechanism relies on the electrostatic interactions between oppositely charged PAA (negative) and PEI (positive) chains[23,24]. These dynamic non-covalent crosslinks enable effective healing through ionic bonds under ambient conditions without external stimuli.

Nonlinear electrical dynamics and applications for multitask recognition

In the HIRE device, the input voltage (V_{IN}) forms a circuit with the ground electrode (GND), and the output voltage (V_{OUT}) is measured on a third electrode via EDL charging–discharging at graphene–hydrogel interfaces (Fig. 2a). Electrochemical impedance spectroscopy revealed that the IN–OUT configuration exhibits approximately double the impedance values compared with the IN–GND and GND–OUT configurations (Fig. 2b). This asymmetry provides the basis for the device's hysteretic behaviour (Extended Data Fig. 1 and Supplementary Note 1). During voltage sweeping, the device exhibited anticlockwise hysteresis with characteristic memcapacitive behaviour (Fig. 2c). A 5 × 5 device array demonstrated consistent hysteresis with device-to-device variations that potentially enhance RC capabilities (Supplementary Fig. 4). The device exhibited short-term plasticity with 98.07% reduction within 2 s in response to a single pulse (Fig. 2d). Tunable plasticity is achieved by varying pulse amplitude and width (Fig. 2e,f). Paired-pulse facilitation behaviour was observed with varying inter-pulse intervals (Fig. 2g). To validate temporal encoding, four-bit binary pulse sequences produced 16 distinct output states (Fig. 2h). Statistical *t*-distributed stochastic neighbor embedding (t-SNE) analysis revealed enhanced state separation, demonstrating the reservoir's ability to transform inputs into higher-dimensional, linearly separable representations (Fig. 2i).

Based on these properties, we implemented a complete RC network (Fig. 3a). Using time multiplexing[25], recurrent connections are established by generating interconnected virtual nodes in the time domain. The preprocessing phase involves feature extraction, fading-memory-based masking[26] and conversion of these features to input-voltage values. The preprocessed inputs were applied to the HIRE, and the voltage outputs of the device were measured as the reservoir states. Output weights (W_{OUT}) are trained via a one-step linear regression in this study. The short-term memory in the HIRE, arising from ion migration, can be accurately described by a two-phase exponential model, as demonstrated in our previous work[27,28] (Extended Data Fig. 2 and Supplementary Note 2). Under stochastic

https://doi.org/10.1038/s41563-026-02532-7

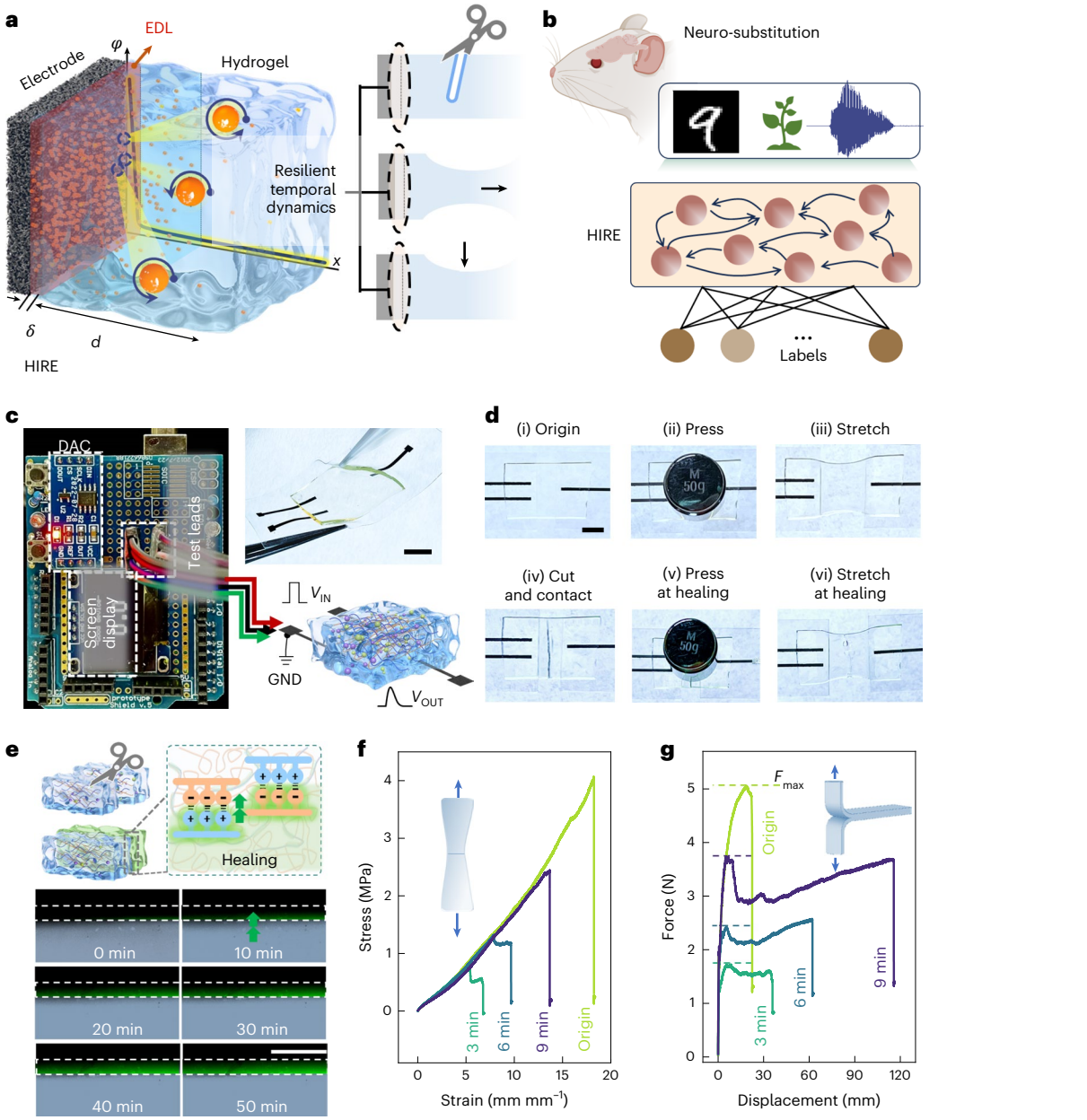

Fig. 1 | Iontronic RC based on SHH. a, Illustration of nanoscale interfacial dynamics within hydrogels, depicting the stern and diffuse layers under mechanical deformations, including cutting, stretching and compression. Φ denotes the electrical potential distribution across the stern and diffuse layers. **b**, Schematic representation of HIRE leveraging nonlinear transformations for higher-order cognitive functions in neuromorphic applications. **c**, Iontronic reservoir device architecture (left), peripheral circuit connections (bottom right) and a photo of the device (top right). Scale bar, 1 cm. **d**, Photographs of the SHH device in six different states: (i) the pristine original device; (ii) the device under a pressed deformation, achieved by placing a 50 g weight onto its surface; (iii) the device under a stretched deformation, corresponding to a 20% elongation from its original length; (iv) the device immediately after being cut and contacted, representing the initial stage of structural healing; and the device first subjected to a deformation of being (v) pressed and then (vi) stretched after healing 3 min, applying the same respective physical conditions (50 g weight for pressing, 20% elongation for stretching). Scale bar, 1 cm. **e**, Schematic diagram illustrating the cutting and healing mechanism of a physically crosslinked PAA/PEI hydrogel. The lower panel shows fluorescence imaging, showing ion migration and crack repair during the healing process. **f**, Mechanical tensile testing of the PAA/PEI hydrogel at different stages of the healing process. The inset shows the hydrogel being stretched. **g**, Representative force–displacement curves obtained from T-peel tests for adhesion strength measurements during structural healing processes. The inset shows the T-peel process. Illustration in **b** created in BioRender; Pei, M. https://biorender.com/0tspt48 (2026).

temporal voltage inputs, the measured V_{OUT} of the HIRE device matches the simulation results based on the device model (Fig. 3b). We performed Mackey–Glass forecasting[29], achieving a root mean square error of ~0.137 (Fig. 3c,d). The device demonstrated over 90% accuracy across nine tasks including spoken digits, hand gestures[30], grasp forces, handwritten digits[31], ovarian structure identification[32], iris classification[33], COVID-19 detection[34–37], electrocardiogram (ECG) diagnosis[38,39] and human action recognition[40] (Fig. 3e and Extended Data Figs. 3–7). Our three-dimensional (3D) mask approach achieved 98.31% accuracy in ECG diagnosis[41]. Detailed methods and results of the prediction and recognition tasks can be found in Supplementary Note 3.

Intelligence restoration and fault tolerance of the system

Biological systems are thought to be more robust than digital systems, and certain creatures can even recover from neural injury and thereby

https://doi.org/10.1038/s41563-026-02532-7

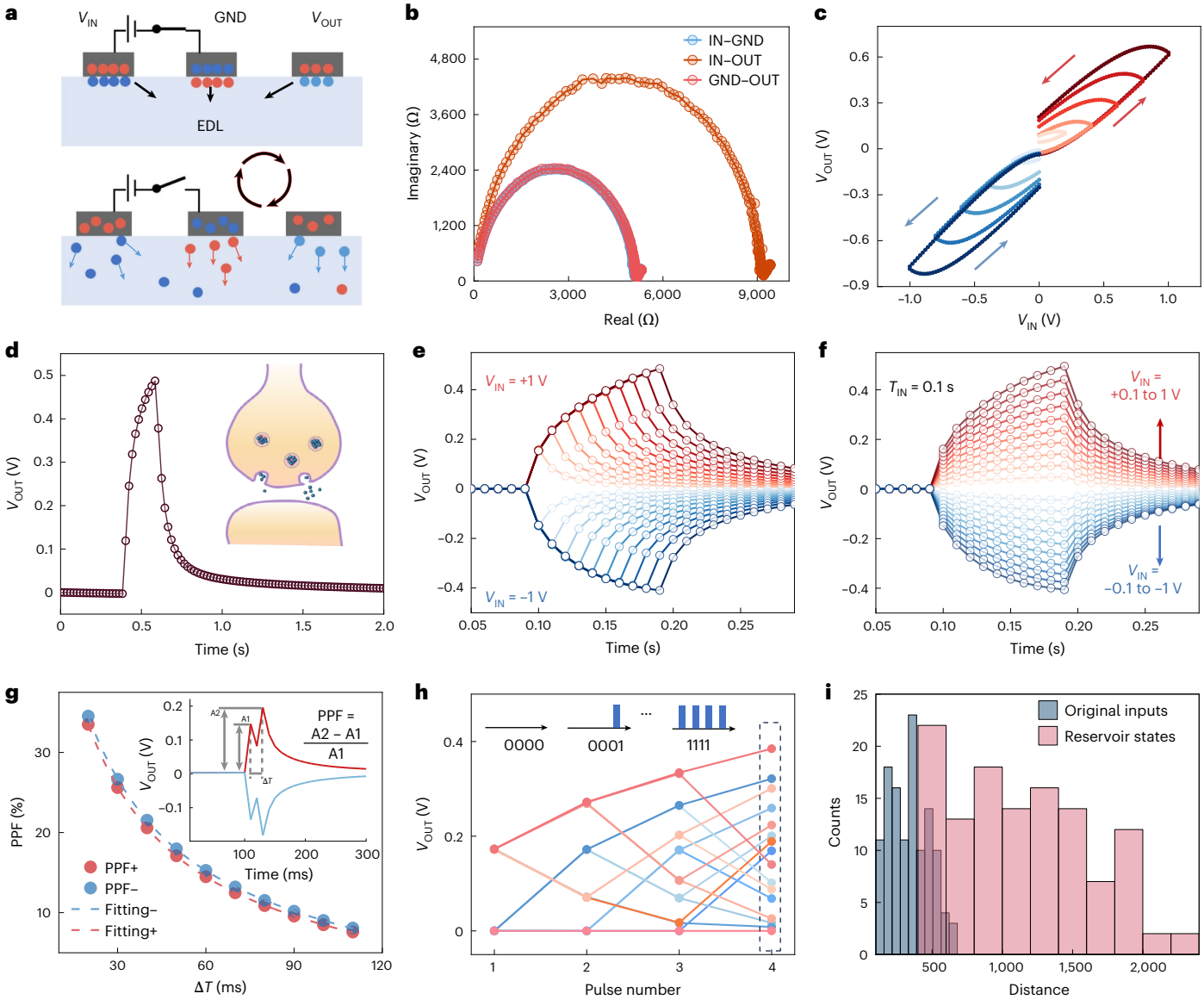

Fig. 2 | Electrical characterization of the HIRE device. a, Schematic illustration of the device operating principle. **b**, Nyquist plots measured between different electrode pairs in the device. **c**, V_{OUT}–V_{IN} hysteresis curves under different voltage sweeping ranges. **d**, Device response to a single input pulse with 200 ms duration and 1 V amplitude. The inset illustrates a biological synapse. **e**, Short-term memory characteristics as a function of pulse duration (±1 V amplitude). **f**, Short-term memory characteristics triggered by electrical pulses of varying amplitudes (pulse duration, T_{IN} = 0.1 s). **g**, Paired-pulse facilitation (PPF) index as a function of inter-pulse interval (ΔT) for positive (+1 V, red) and negative (−1 V, blue) pulse amplitudes. Dashed curves represent double-exponential decay function fits. The inset shows the PPF response triggered by two successive presynaptic spikes with ΔT = 20 ms. **h**, Device response to temporal sequence encodings ranging from 0000 to 1111 (1: 1 V, 100 ms; 0: 0 V, 100 ms). **i**, Statistical analysis of distances in t-SNE results.

rehabilitate their cognitive functions. For example, *Octopus vulgaris* is well known for the capacity to regenerate central and peripheral nervous systems distributed in arms and other body parts (Fig. 4a). The process involves wound healing, followed by proliferation of pluripotent precursor cells into a blastema[42]. These cells regenerate neurons and restore sensory and motor functions within days to months. Surgical limb reattachment can further expedite this process by facilitating precise neural connections[43].

To quantify the electrical healing kinetics that are the key to functional recovery, the output signal was monitored during a cut-and-heal cycle of the HIRE device (Fig. 4b). A voltage pulse (1 V, 4.5 s) was applied to the intact device to establish a baseline electrical response. The device was then completely cut, causing the output signal to be abruptly disrupted and replaced by noise. Upon recontacting the cutting surfaces, the output signal recovered to its original level in approximately 0.02 s. Notably, the subsequent decay profile of the restored signal perfectly matched that of the pristine device, confirming full and accurate functional restoration. Physically cutting off the hydrogel disrupts the conductive ionic pathway, thereby electrically isolating the electrodes (Supplementary Fig. 6). However, upon recontact, the ionic continuum is immediately restored through electrostatic coupling. Therefore, the restoration does not depend on the slower structural healing (polymer chain diffusion) process as characterized in Fig. 1e, but on the near-instantaneous re-establishment of the electrostatic field. This mechanism decouples functional recovery from structural healing, presenting a notable advantage. Specifically, most self-healing systems rely on slow reformation of chemical or physical bonds and mechanical strength for functional restoration, with recovery times ranging from minutes to hours. Our device achieves the functional restoration in tens of milliseconds, which is orders of magnitude faster.

https://doi.org/10.1038/s41563-026-02532-7

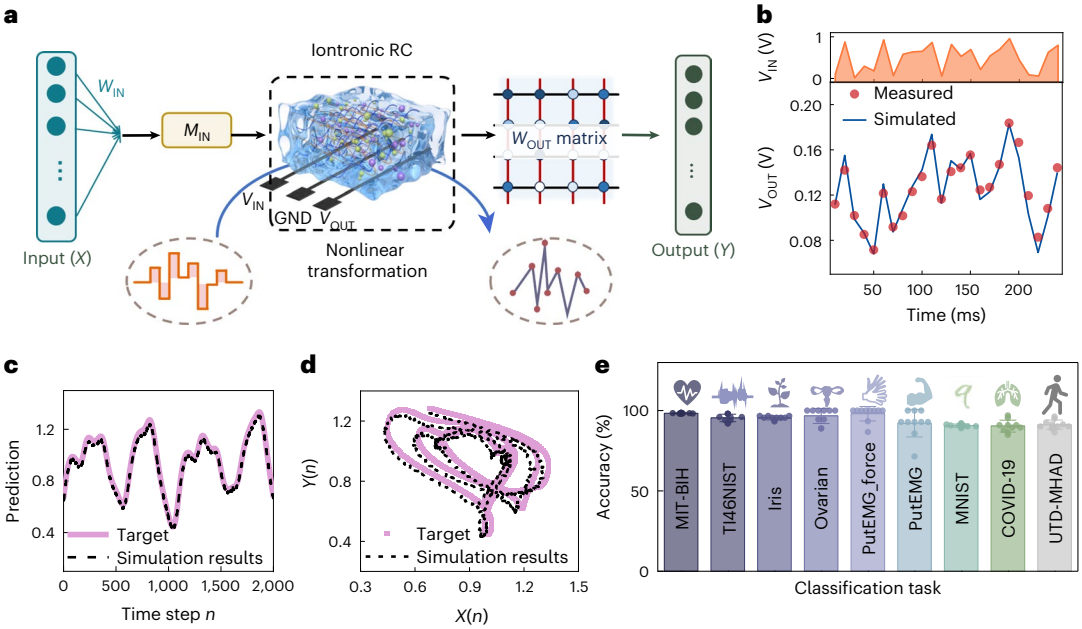

Fig. 3 | Architecture and simulation validation of the HIRE-based RC network. **a**, Schematic of the HIRE-based RC network. The system used the ion migration processes in the hydrogel to obtain the reservoir state and operated the linear regression through a memristor crossbar array to get the final output. W_{IN} and M_{IN} are the input weight and input mask, respectively. **b**, The measured voltage output of the HIRE device and simulation results based on the device model. **c**, Forecasting results of the Mackey–Glass time series. The pink line represents the real data to estimate, and the black dotted line represents the predicted output based on the device model. **d**, Two-dimensional (2D) display of the predicted results. *X* and *Y* are functions of *n*. **e**, Classification accuracy for nine different intelligent tasks using standard datasets. MIT-BIH, Massachusetts Institute of Technology–Beth Israel Hospital arrhythmia database; TI46NIST, Texas Instruments 46-word speech corpus; Iris, Fisher's Iris dataset; Ovarian, ovarian cancer dataset; PutEMG and PutEMG-force, electromyography datasets from the Poznan University of Technology; MNIST, Modified National Institute of Standards and Technology database of handwritten digits; COVID-19, COVID-19 radiography dataset. UTD-MHAD, University of Texas at Dallas Multimodal Human Action Dataset. Data are presented as mean values ± s.d. with $n = 10$ (10-fold cross-validation).

The electrical performance, including V_{OUT}–V_{IN} hysteresis loops, pulse responses and nonlinear mapping of four-bit inputs, was characterized during the six physical states as mentioned in Fig. 1d (Supplementary Fig. 7), indicating preservation of electrical performance during structural healing. The memory capacity was calculated to assess its temporal information-processing capabilities for all six device states. As a fundamental metric in RC, memory capacity reflects the system's ability to retain and process temporal dependencies in input signals. Here, three representative tasks were applied: short-term memory, parity check and XOR. These tasks represent varying levels of complexity and temporal dependency, providing a robust framework to assess the system's performance (details of these tasks can be found in Supplementary Note 4). Statistical analysis of memory capacity for these tasks (Fig. 4c) shows no statistically significant differences, confirming the preservation of temporal processing capabilities under physical deformation throughout the structural healing processes. The energy consumption was estimated to be 1.64×10^{-5} nJ μm^{-2} per spike, which is comparable to other low-energy-consumption reservoir devices (Supplementary Table 2 and Supplementary Fig. 8).

The HIRE device was applied to verify the restoration of intelligent functionality in practical scenarios (Supplementary Fig. 9). The system collected 200 speech signals (cancel, confirm, up and down commands, with each command represented by 50 signals) and achieved 90% accuracy in the speech-recognition task (Supplementary Figs. 10 and 11; Supplementary Video 2 and the Methods include the detailed procedure). Next, the HIRE device was cut into two separate parts and then reattached. Spoken recognition tasks were implemented to validate the RC capability during the healing process. As the input and output electrodes are positioned on opposite sides of the split, the system is out of work after cutting the HIRE device. As a result, the recognition accuracy of the system drops to 25% when using the original W_{OUT} (Supplementary Fig. 12). During the reconnection, the spoken recognition tasks were performed at four device states during the healing process (Fig. 4d): (1) just at the reattachment (-0.02 s); (2) 180 s after reattachment under an applied press; (3) after recovery from the press condition, under an applied stretch at 180 s after reattachment; and (4) 540 s after reattachment (structural recovery almost completed). Just at the reattachment of the fractured SHH surfaces, a high accuracy of 95% was achieved (Fig. 4e). After 540 s, the accuracy of the spoken recognition task was 90% (Fig. 4f), which is close to that of the initial state. Throughout the entire recognition evaluation process across all four device states, the original W_{OUT} was used without retraining. This enables time-efficient recovery of processing capability, as no additional retraining time is required after the healing of HIRE devices. This property is derived from the inherent fault tolerance to parametric variations during fracture recovery processes in the HIRE-based RC system. Despite minor numerical variations in the output for identical signals, the HIRE consistently maintains a high-dimensional mapping of the input signals, like the fuzzy computing mechanisms in the human brain[44]. The neuromorphic healing speed of the HIRE-based RC system is several orders of magnitude faster than that of existing self-healing neuromorphic devices and creatures in terms of neuronal or neuron-like function restoration[17,45–50] (Fig. 4g and Supplementary Table 3). More importantly, our HIRE-based RC system demonstrates intelligent task recovery, showing restorable intelligence and moving a step closer to the intelligence of creatures.

Implantable reservoir for closed-loop neural stimulation control

The bio-inspired restorable intelligence makes HIREs particularly promising for implantable neural substitution applications. To demonstrate practical biomedical applications, we implanted the HIRE

https://doi.org/10.1038/s41563-026-02532-7

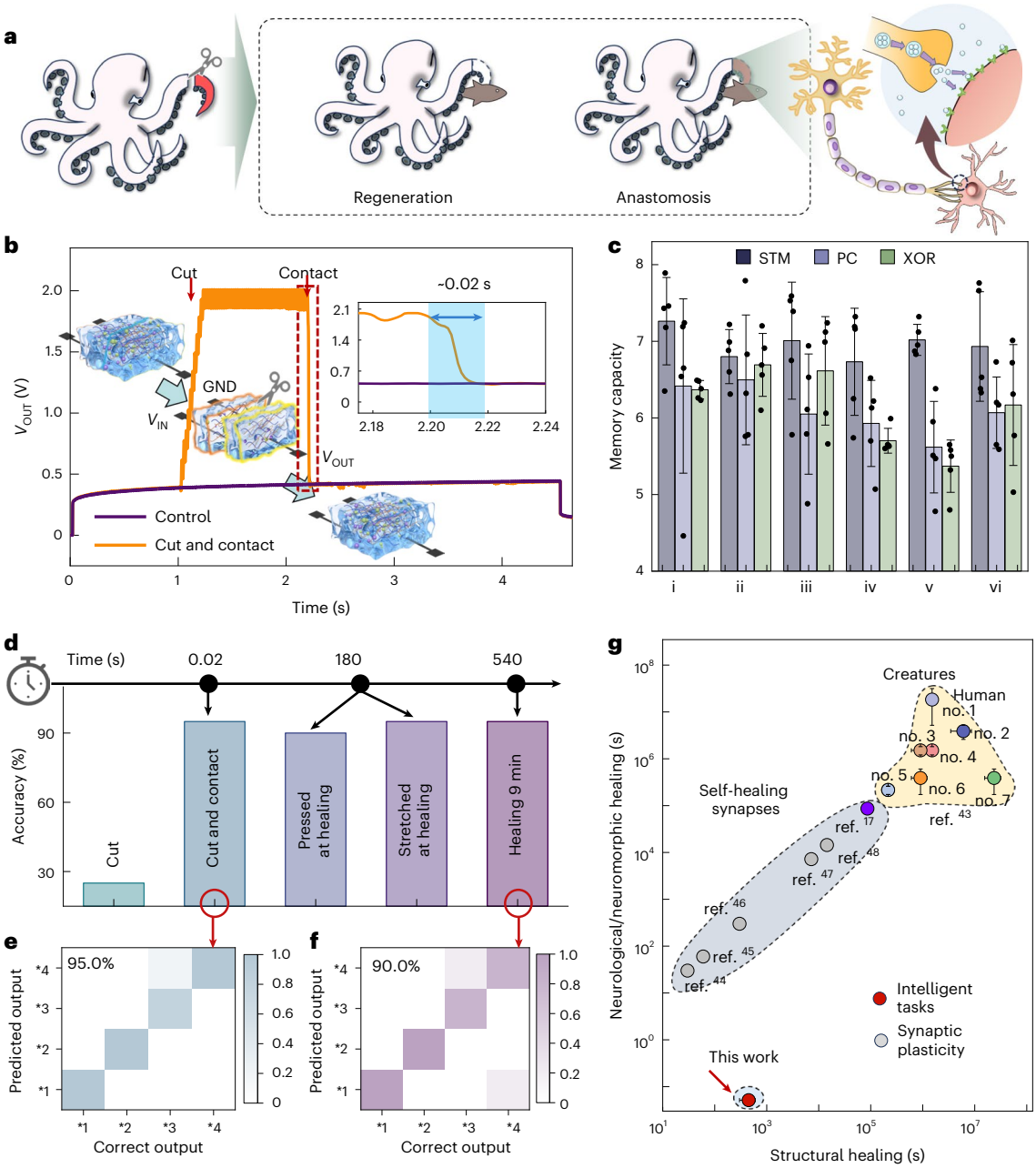

Fig. 4 | Restoration of intelligent tasks in the HIRE-based RC network. **a**, Illustration of intelligent rehabilitation in an octopus via regeneration or therapy (anastomosis), both leading to cognitive recovery. **b**, Electrical measurements during cutting and functional healing processes. The inset illustrates a cut-and-heal cycle of the HIRE device. **c**, Statistical comparison of memory capacity across different computational tasks, including parity check (PC), short-term memory (STM) and XOR operations, evaluated in six different physical states. Data are presented as mean values ± s.d. The sample size $n = 5$ represents five independent measurement trials performed on the same device. **d**, Computational performance for speech-recognition task at different times of the healing process. Speech labels of down, up, cancel and confirm are denoted by *1–*4, respectively. **e**, Speech-recognition results (confusion matrix) for tasks performed immediately after reattaching the fractured SHH surfaces, achieving 95.0% recognition accuracy. **f**, Speech-recognition results (confusion matrix) after substantial structural healing for 540 s, achieving 90.0% recognition accuracy. **g**, Comparison of time requirements for neurological/neuromorphic and structural healing between the HIRE and existing neuromorphic devices and biological organisms. Nos 1–7 correspond to human, axolotl, zebrafish, sea squirt, fruit fly and hydra, planarian and starfish, respectively. Data are presented as mean ± s.d. calculated from the upper and lower bounds of the parameters reported in the literature[45–50].

devices for closed-loop neural stimulation control in rehabilitation exercises. Our approach integrates external voice commands with internal physiological monitoring to address critical limitations in current rehabilitation approaches (Fig. 5a). Rehabilitation exercises and/or therapeutic stimulations are required for recovery from certain illnesses or surgeries to restore impaired sensorimotor function[51]. However, patients may not be aware of their physiological state by simply following standardized protocols. Closed-loop systems of neural interfaces represent an advanced form of neuromodulation characterized by real-time monitoring of neural activity to dynamically adjust therapeutic stimulation[52]. This adaptive approach enables precise, targeted interventions for applications such as symptom management and motor function restoration. The first step in achieving a closed-loop neural stimulation control is to establish the indicator for monitoring internal physiological states. For example, local muscle pH can serve as an indicator of fatigue level during exercise, as pH changes reflect

https://doi.org/10.1038/s41563-026-02532-7

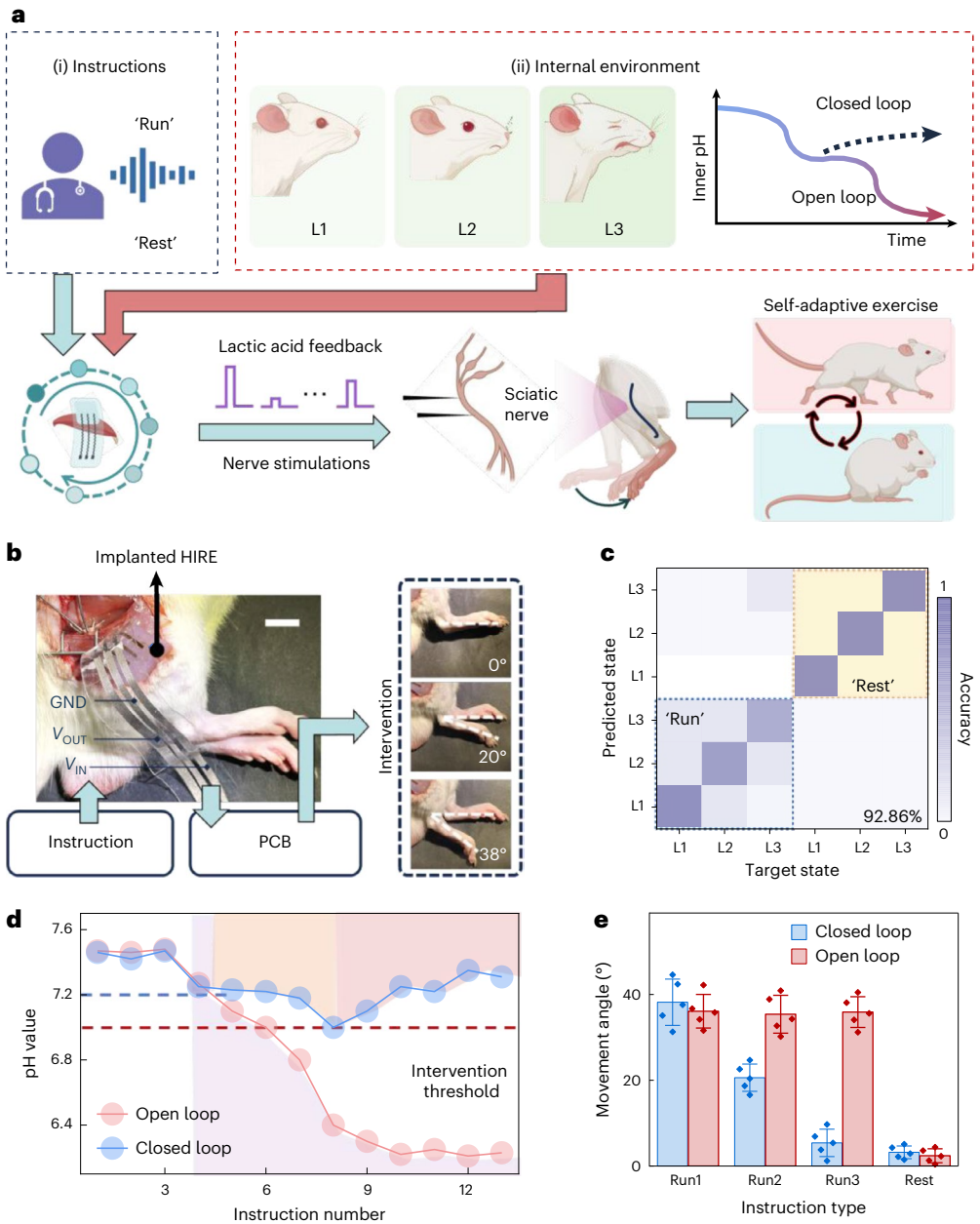

Fig. 5 | The HIRE-based neuromorphic prosthesis. a, Schematic illustration of HIRE-based neuromorphic prosthesis. **b**, Photograph of the HIRE device implanted near the rat leg muscle. Voice commands are processed by the device in the rat leg, and the recognition results are transmitted through a printed circuit board (PCB) to generate corresponding stimulation signals for the rat sciatic nerve, inducing leg movement with different angles. **c**, Confusion matrix of recognition results, where labels L1, L2 and L3 correspond to pH environments of 7.4, 7.2 and 7.0, respectively. **d**, pH variation trends on the rat leg muscle surface under open-loop and closed-loop control. The shaded regions indicate different command states during closed-loop operation: Run1 (purple), Run2 (yellow) and Run3 (red), corresponding to stimulation amplitudes of 5 V, 4 V and 3 V, respectively. The horizontal dashed lines represent the pH thresholds used for physiological state classification, with the blue dashed line at pH 7.2 and the red dashed line at pH 7.0. **e**, Statistical analysis of rat leg movement angles corresponding to open-loop and closed-loop commands. Data are presented as mean values ± s.d. Measurements were taken five times under each instruction. Illustration in **a** created in BioRender; Pei, M. https://biorender.com/kfnnk4a (2026).

the physiological correlate of lactic acid accumulation during muscle exertion. With increasing motor activity, patients transition through different fatigue levels, leading to drops in internal pH. We defined three physiological states for this study (L1, well-rested, pH 7.4; L2, moderately exerted, pH 7.2; L3, fatigued, pH 7.0). Importantly, our HIRE devices have demonstrated pH-sensitive ionic dynamics (details are in Extended Data Fig. 8 and Supplementary Note 5), enabling simultaneous voice command recognition and fatigue detection.

The implanted HIRE device is positioned near the target muscle to interact with the surrounding microenvironment. The recognition results are then converted to stimulate the sciatic nerves of a rat (Extended Data Fig. 9a). The stimulation was applied to the sciatic nerve using bipolar hook electrodes (3 mm spacing) with 100 electrical pulses at a 67% duty cycle and 5 Hz frequency. In this case, the rat would keep running (or rest) after the HIRE-based RC system receives the command of 'Run' (or 'Rest'), which mimics the situation of rehabilitation exercises based on the doctor's advice. The pulse amplitude can be changed to control the leg movement angle (θ_{leg}), corresponding to the different intensities of leg movements. Pulse amplitudes of 5 V, 4 V and 0 V produced movements of 38°, 20° and 0°, respectively (Fig. 5b).

If the pulse amplitudes are fixed, the process of exercise intensity control is noted as 'open-loop', which would lead to continuous pH decline and potential acidosis.

To achieve the closed-loop neural stimulation control, the HIRE-based RC system was trained to classify six distinct states, combining voice commands with physiological conditions (Supplementary Fig. 13). The SHH device exhibits distinct responses to identical time-series inputs under different pH conditions during voice command recognition tasks (Extended Data Fig. 9b). Testing across all pH conditions demonstrated a high classification accuracy of 92.86% (Fig. 5c), confirming reliable voice command recognition under varying physiological states. Comparative experiments were conducted between open-loop and closed-loop control modes (Extended Data Fig. 9c). The open-loop control system assumes that the rat remains in a well-rested state after receiving a 'Run' command with a stimulation amplitude of 5 V, regardless of the actual muscle state, while the closed-loop control system dynamically adjusts stimulations in response to different muscle states. Each command was applied for 10 s intervals, during which pH measurements were taken using a handheld pH meter. Under closed-loop control (Fig. 5d), when the pH dropped to 7.2, the system automatically recognized that the rat was in a moderate state (Run2) and reduced stimulation amplitude to 4 V, resulting in decreased movement intensity and a slower rate of pH decline. When the pH further decreased to 7.0, the system identified a fatigued state (Run3) and reduced stimulation to 3 V, resulting in minimal leg movement and gradual pH recovery. Statistical analysis of leg movement angles revealed that the first amplitude reduction decreased movement from 38.2 ± 5.4° to 20.6 ± 3.2°, while under Run3 conditions, leg movement angles (5.4 ± 3.4°) were close to those during rest commands (3.2 ± 1.5°; Fig. 5e). By contrast, the open-loop system maintained continuous high-intensity leg movements ($\theta_{leg} > 35°$), causing rapid lactic acid accumulation and sustained pH decline. Without adaptive control intervention, such excessive exercise induces acidosis, which is detrimental to motor rehabilitation.

In addition, a biomedical safety assessment confirmed that the HIRE maintains biocompatibility during implantation (Extended Data Fig. 9d–f and Supplementary Note 6). Soft HIRE devices were fabricated using LIG electrodes on polydimethylsiloxane (PDMS) substrates (Supplementary Fig. 14). Device modelling validated nine intelligent tasks with >90% accuracy (Extended Data Fig. 10).

This HIRE-based neuromorphic prosthesis offers transformative potential for sensorimotor rehabilitation by enabling intuitive voice-controlled muscle activation for patients with motor impairments while maintaining biocompatibility and adaptive functionality in dynamic biological environments. The system simplifies sensing components and related processing circuits, offering an energy-efficient and lightweight implantable intelligent platform. Our work not only mimics neuronal rehabilitation with self-healing intelligence but also reveals the potential for sensorimotor function restoration and other medical applications, providing a compact, biocompatible solution that establishes a foundation for next-generation neural prosthetics and autonomous bioelectronic medicine.

Outlook

This work reports a HIRE that demonstrates exceptional physical and functional robustness and enables adaptive closed-loop neural stimulation control in neuromorphic prostheses. This platform would advance robustness and functionality in implantable devices and neuro-substitutions. Future development relies on certain aspects of the platform.

At the material level, the PAA/PEI hydrogels combine mechanical robustness and biocompatibility. The ionic crosslinking mechanism ensures rapid self-healing without external stimuli, maintaining both structural and functional integrity. Beyond traditional applications, the rich ion dynamics provide the potential for neuromorphic computing. Additionally, the hydrogels' biocompatibility avoids cytotoxicity and immune reactions, enabling safe and long-term implantation. These properties make hydrogels ideal for next-generation neuroprosthetics and bio-hybrid systems that maintain reliable performance under dynamic conditions in biological environments.

At the device level, our reservoir device, based on a three-terminal planar memcapacitor, confines the critical functional layer within the nanoscale, minimizing structural damage impacts compared with bulk-governed reservoirs like memristors and transistors. In those devices, temporal dynamics rely on cross-dielectric ion migration or channel carrier dynamics, involving larger dimensions and multiple materials more vulnerable to structural failure. Moreover, restoring bulk-based devices would require complex recovery of dielectric and semiconductor layers. By contrast, our device rapidly restores functions by reattaching fractured surfaces without additional alignment. Therefore, HIRE devices are well-suited for use in mechanically harsh environments, providing a solid device foundation for robust and fault-tolerant computation.

At the computational level, RC emulates the fuzzy, nonlinear dynamics of biological neural networks, which are fault tolerant to perturbations in both inputs and parameters of the network[53,54]. Specifically, the brain is assumed to be a nonlinear system throughout all spatial and temporal scales in neuroscience, where intricate networks of neurons and synapses inherently exhibit stochastic behaviour[55]. Similarly, our HIRE-based RC network can tolerate a certain level of numerical changes due to structural defects induced by cutting and healing. Such high robustness also facilitates the immediate restoration of neuromorphic computing, as no retraining or calibration, such as adjusting the output weight matrix, is required. This improves time efficiency for restoration, thereby avoiding complex replacement surgery and reducing the survival risk from temporal incapacitation.

In conclusion, iontronic RC was implemented in a SHH-based memcapacitor, which exhibited a highly efficient and robust neuromorphic computing capability. Such reservoir devices have been demonstrated with a high tolerance to mechanical disruptions and enable immediate restoration of temporal dynamics without requiring external stimuli or recalibration. The RC system built on a HIRE achieved high accuracies, exceeding 90% across nine benchmark tasks through simulations. The HIRE verified time-efficient (~0.02 s) restoration and biomedical safety by implementing speech-recognition tasks. The closed-loop neural stimulation control capability based on pH-modulated dynamics in the HIRE further establishes the clinical relevance of this technology for therapeutic applications. This work marks a substantial advancement towards next-generation neuro-substitutions, addressing key challenges in both neuromorphic engineering and biomedical innovation.

Online content

Any methods, additional references, Nature Portfolio reporting summaries, source data, extended data, supplementary information, acknowledgements, peer review information; details of author contributions and competing interests; and statements of data and code availability are available at https://doi.org/10.1038/s41563-026-02532-7.

References

1. Harikesh, P. C. et al. Ion-tunable antiambipolarity in mixed ion–electron conducting polymers enables biorealistic organic electrochemical neurons. *Nat. Mater.* **22**, 242–248 (2023).
2. Sarkar, T. et al. An organic artificial spiking neuron for in situ neuromorphic sensing and biointerfacing. *Nat. Electron.* **5**, 774–783 (2022).
3. Keene, S. T. et al. A biohybrid synapse with neurotransmitter-mediated plasticity. *Nat. Mater.* **19**, 969–973 (2020).
4. Kim, Y. et al. A bioinspired flexible organic artificial afferent nerve. *Science* **360**, 998–1003 (2018).

5. Lee, Y. et al. A low-power stretchable neuromorphic nerve with proprioceptive feedback. *Nat. Biomed. Eng.* **7**, 511–519 (2023).
6. Soman, S., Jayadeva & Suri, M. Recent trends in neuromorphic engineering. *Big Data Anal.* **1**, 15 (2016).
7. Mead, C. How we created neuromorphic engineering. *Nat. Electron.* **3**, 434–435 (2020).
8. Zenke, F. et al. Visualizing a joint future of neuroscience and neuromorphic engineering. *Neuron* **109**, 571–575 (2021).
9. Indiveri, G. & Horiuchi, T. K. Frontiers in neuromorphic engineering. *Front. Neurosci.* **5**, 118 (2011).
10. Harmon, L. D. Artificial neuron. *Science* **129**, 962–963 (1959).
11. Tang, J. et al. Bridging biological and artificial neural networks with emerging neuromorphic devices: fundamentals, progress, and challenges. *Adv. Mater.* **31**, 1902761 (2019).
12. Chen, S., Zhang, T., Tappertzhofen, S., Yang, Y. & Valov, I. Electrochemical-memristor-based artificial neurons and synapses—fundamentals, applications, and challenges. *Adv. Mater.* **35**, 2301924 (2023).
13. Wang, T. et al. A chemically mediated artificial neuron. *Nat. Electron.* **5**, 586–595 (2022).
14. Cao, Y. et al. Self-healing electronic skins for aquatic environments. *Nat. Electron.* **2**, 75–82 (2019).
15. Kang, J., Tok, J. B.-H. & Bao, Z. Self-healing soft electronics. *Nat. Electron.* **2**, 144–150 (2019).
16. Vo, N. T. P. et al. Autonomous self-healing supramolecular polymer transistors for skin electronics. *Nat. Commun.* **15**, 3433 (2024).
17. John, R. A. et al. Self healable neuromorphic memtransistor elements for decentralized sensory signal processing in robotics. *Nat. Commun.* **11**, 4030 (2020).
18. Stojek, Z. in *Electroanalytical Methods: Guide to Experiments and Applications* (eds Scholz, F. et al.) 3–9 (Springer, Berlin, Heidelberg, 2010).
19. Bohinc, K., Kralj-Iglič, V. & Iglič, A. Thickness of electrical double layer. Effect of ion size. *Electrochim. Acta* **46**, 3033–3040 (2001).
20. Saboorian-Jooybari, H. & Chen, Z. Calculation of re-defined electrical double layer thickness in symmetrical electrolyte solutions. *Results Phys.* **15**, 102501 (2019).
21. Tsunegi, S. et al. Physical reservoir computing based on spin torque oscillator with forced synchronization. *Appl. Phys. Lett.* **114**, 164101 (2019).
22. Everschor-Sitte, K., Majumdar, A., Wolk, K. & Meier, D. Topological magnetic and ferroelectric systems for reservoir computing. *Nat. Rev. Phys.* **6**, 455–462 (2024).
23. Virgen-Ortíz, J. J. et al. Polyethylenimine: a very useful ionic polymer in the design of immobilized enzyme biocatalysts. *J. Mater. Chem. B* **5**, 7461–7490 (2017).
24. Naficy, S., Spinks, G. M. & Wallace, G. G. Thin, tough, pH-sensitive hydrogel films with rapid load recovery. *ACS Appl. Mater. Interfaces* **6**, 4109–4114 (2014).
25. Appeltant, L. et al. Information processing using a single dynamical node as complex system. *Nat. Commun.* **2**, 468 (2011).
26. Pei, M. et al. Power-efficient multisensory reservoir computing based on Zr-doped HfO_2 memcapacitive synapse arrays. *Adv. Mater.* **35**, 2305609 (2023).
27. Yang, Y. et al. Reservoir computing based on electric-double-layer coupled InGaZnO artificial synapse. *Appl. Phys. Lett.* **122**, 043508 (2023).
28. Williams, G. & Watts, D. C. Non-symmetrical dielectric relaxation behaviour arising from a simple empirical decay function. *Trans. Faraday Soc.* **66**, 80–85 (1970).
29. Doyne Farmer, J. Chaotic attractors of an infinite-dimensional dynamical system. *Phys. D* **4**, 366–393 (1982).
30. Kaczmarek, P., Mańkowski, T. & Tomczyński, J. putEMG—a surface electromyography hand gesture recognition dataset. *Sensors* **19**, 3548 (2019).
31. Lecun, Y., Bottou, L., Bengio, Y. & Haffner, P. Gradient-based learning applied to document recognition. *Proc. IEEE* **86**, 2278–2324 (1998).
32. Conrads, T. P. et al. High-resolution serum proteomic features for ovarian cancer detection. *Endocri. Relat. Cancer* **11**, 163–178 (2004).
33. Fisher, R. A. The use of multiple measurements in taxonomic problems. *Ann. Eugen.* **7**, 179–188 (1936).
34. Rahman, T. COVID-19 Radiography Database. *Kaggle* https://www.kaggle.com/datasets/tawsifurrahman/covid19-radiography-database (2026).
35. Kermany, D. S. et al. Identifying medical diagnoses and treatable diseases by image-based deep learning. *Cell* **172**, 1122–1131.e9 (2018).
36. Chowdhury, M. E. H. et al. Can AI help in screening viral and COVID-19 pneumonia? *IEEE Access* **8**, 132665–132676 (2020).
37. Tawsifur, R. A. et al. Exploring the effect of image enhancement techniques on COVID-19 detection using chest X-ray images. *Comput. Biol. Med.* https://doi.org/10.1016/j.compbiomed.2021.104319 (2021).
38. Zhong, Y. et al. A memristor-based analogue reservoir computing system for real-time and power-efficient signal processing. *Nat. Electron.* **5**, 672–681 (2022).
39. Goldberger, A. L. et al. PhysioBank, PhysioToolkit, and PhysioNet: components of a new research resource for complex physiologic signals. *Circulation* **101**, E215–E220 (2000).
40. Chen, C., Jafari, R. & Kehtarnavaz, N. UTD-MHAD: a multimodal dataset for human action recognition utilizing a depth camera and a wearable inertial sensor. In *2015 IEEE International Conference on Image Processing (ICIP)* 168–172 (IEEE, 2015).
41. Liu, D. et al. A wearable in-sensor computing platform based on stretchable organic electrochemical transistors. *Nat. Electron.* **7**, 1176–1185 (2024).
42. Imperadore, P., Shah, S. B., Makarenkova, H. P. & Fiorito, G. Nerve degeneration and regeneration in the cephalopod mollusc *Octopus vulgaris*: the case of the pallial nerve. *Sci. Rep.* **7**, 46564 (2017).
43. Barbary, S., Dap, F. & Dautel, G. Finger replantation: surgical technique and indications. *Chir. Main* **32**, 363–372 (2013).
44. Kadak, U. Modeling brain information flow dynamics with multidimensional fuzzy inference systems. *Inf. Sci.* **677**, 120807 (2024).
45. Arenas Gómez, C. M., Sabin, K. Z. & Echeverri, K. Wound healing across the animal kingdom: crosstalk between the immune system and the extracellular matrix. *Dev. Dyn.* **249**, 834–846 (2020).
46. Wang, F. et al. Self-healing memristors based on SA/PVA/STB hydrogel. *J. Mater. Sci. Mater. Electron.* https://doi.org/10.1007/s10854-023-10942-5 (2023).
47. Wang, K. et al. A biodegradable, stretchable, healable, and self-powered optoelectronic synapse based on ionic gelatins for neuromorphic vision system. *Small* **20**, 2404566 (2024).
48. Gao, Y. et al. Artificial synapses based on organic electrochemical transistors with self-healing dielectric layers. *Chin. Chem. Lett.* **35**, 108582 (2024).
49. Qiu, R. et al. Bilingual bidirectional stretchable self-healing neuristors with proprioception. *ACS Nano* **17**, 12652–12662 (2023).
50. Han, S. et al. An antifatigue and self-healable ionic polyurethane/ionic liquid composite as the channel layer for a low energy cost synaptic transistor. *Eur. Polym. J.* **174**, 111292 (2022).

51. Van Der Werf, J., Buchholz, V. N., Jensen, O. & Medendorp, W. P. Neuronal synchronization in human parietal cortex during saccade planning. *Behav. Brain Res.* **205**, 329–335 (2009).
52. Shoaran, M. Next-generation closed-loop neural interfaces: circuit and AI-driven innovations. *IEEE Solid State Circuits Mag.* **15**, 41–49 (2023).
53. Zlokapa, A. et al. Fault-tolerant neural networks from biological error correction codes. *Phys. Rev. E* **110**, 054303 (2024).
54. Ichinose, N., Kawashima, T., Yada, T. & Wada, H. Dynamical robustness and its structural dependence in biological networks. *J. Theor. Biol.* **526**, 110808 (2021).
55. Deco, G., Rolls, E. T. & Romo, R. Stochastic dynamics as a principle of brain function. *Prog. Neurobiol.* **88**, 1–16 (2009).

[1]School of Electronic Science and Engineering, National Laboratory of Solid-State Microstructures, Nanjing University, Nanjing, P. R. China. [2]Collaborative Innovation Center of Advanced Microstructures, School of Physics, Nanjing University, Nanjing, China. [3]Department of Radiology, Jinling Hospital, Affiliated Hospital of Medical School, Nanjing University, Nanjing, China. [4]Institute of Materials Research and Engineering (IMRE), Agency for Science, Technology and Research (A*STAR), Singapore, Singapore. [5]Innovative Center for Flexible Devices (iFLEX), Max Planck-NTU Joint Laboratory for Artificial Senses, School of Materials Science and Engineering, Nanyang Technological University, Singapore, Singapore. [6]Key Laboratory for Organic Electronics and Information Displays and Jiangsu Key Laboratory for Biosensors, Institute of Advanced Materials, Jiangsu National Synergetic Innovation Centre for Advanced Materials, Nanjing University of Posts and Telecommunications, Nanjing, P. R. China. [7]Yongjiang Laboratory (Y-LAB), Ningbo, China. [8]These authors contributed equally: Mengjiao Pei, Tian Gao, Li Liu. ✉e-mail: yli@nju.edu.cn; xuebinnju@nju.edu.cn; yshi@nju.edu.cn; wanqing@nju.edu.cn; chenxd@ntu.edu.sg; cjwan@nju.edu.cn

Methods

Material preparation

Ethylene imine polymer (PEI; molecular weight M_w = 70,000) aqueous solution (50 wt%) and acrylic acid (AR, >99% purity as determined by gas chromatography (GC), contains 180–200 ppm monomethyl ether of hydroquinone (MEHQ) as inhibitor) were purchased from Aladdin. Lithium phenyl (2,4,6-trimethylbenzoyl) phosphinate (LAP) was purchased from TCI Shanghai. Isoflurane was purchased from Yuyan Scientific Instrument Co.

Preparation and characterization of PAA/PEI hydrogels

The synthesis of PAA/PEI hydrogels commenced with the dissolution of PEI (2 mg ml^{-1}) and acrylic acid (400 mg ml^{-1}) in deionized water. To eliminate dissolved oxygen, the mixture was purged with argon gas in three 15 min intervals. Subsequently, ammonium LAP (0.5 mg ml^{-1}) was introduced as a photoinitiator. The polymerization reaction proceeded under blue light (405 nm) at ambient temperature (22 °C) for 2 h, resulting in the formation of PAA/PEI hydrogels. The mechanical properties of the hydrogels, specifically the tensile stress–strain relationships, were determined at room temperature in ambient conditions using an Instron-5944 tensile-compressive tester equipped with a 10 N load cell. The stretching rate was consistently held at approximately 10 mm min^{-1}. The strain was calculated as the ratio of displacement between the clamps in the stretched state to that in the unstretched state. In the self-healing experiments, sections of SHH bands were severed and then aligned and compressed together at room temperature. This facilitated self-healing without the need for external interventions. During characterization of fluorescence migration, 0.1 mg ml^{-1} of fluorescein *o*-acrylate (CAS no. 193419) was induced into one of the hydrogel precursor solutions. T-peel tests were performed on the hydrogel samples. For the experiment, hydrogel samples were precisely cut along their midline into two halves, each with a width (W) of 7–8 mm. The cut surfaces were then carefully brought into contact to initiate the self-healing process, and subsequent peel tests were conducted after various self-healing times. The 'Origin' group served as a crucial control, representing an intact hydrogel sample that was only partially cut (halfway through the sample width) to retain a continuous connection at the rear, allowing us to assess the maximum force (F_{max}) of a near-pristine sample.

Device fabrication and characterization

Polyimide films (Kapton, 125 µm thickness) were cleaned with ethanol and adhered to optical glass substrates to prevent thermal deformation during laser processing. LIG electrodes were fabricated using a commercial 5 W, 355 nm ultraviolet laser (Lixia), with patterns designed in vector graphics software. Laser parameters were optimized at 150 kHz frequency, 6 µs pulse width and 150 mm s^{-1} scan speed, with the laser head positioned 3 mm above the substrate surface to ensure optimal graphene formation through direct material interaction.

For implantable soft devices, the polyimide thickness was reduced to 22 µm to enhance flexibility. Following initial electrode patterning, edge cutting was performed with focused laser positioning to precisely define electrode geometries and achieve concentrated energy delivery for clean pattern definition. The remaining polyimide film connections were then severed, and the substrate was immersed in ethanol solution for 30 min to dissolve the adhesive interface between the polyimide and glass, enabling natural separation. Device assembly was completed by carefully transferring the LIG electrodes to PDMS substrates using tweezers, followed by hydrogel deposition at the electrode terminals. For standard devices, the hydrogel was directly adhered to the polyimide substrate with prefabricated LIG electrodes.

Electrochemical tests were performed using a CHI660C electrochemical workstation (Shanghai Chenhua Instrument Co.). The electrochemical impedance spectroscopy measurements were carried out within a frequency range of 100 kHz to 0.1 Hz, applying a voltage amplitude of 5 mV. The electrical performances of the memcapacitor device were measured by a semiconductor parameter analyser (PDA FS380 Pro, Platform Design Automation) in a probe station. Three probes were connected to the V_{IN}, GND and V_{OUT} electrodes, respectively. These probes were connected to the three Medium Power Source/Measure Unit (MPSMU) ports, with a current source output resistance of at least 10^{13} Ω. The accurate and precise measurement ranges were 0.1 fA to 1 A and 0.5 µV to 200 V. The output capacitance of our set-up was 1,000 pF (1 pA to 10 nA ranges).

Characterizations of the HIRE-based network

During training, the collected signals undergo feature extraction and masking in MATLAB (R2022b) before being input into the HIRE to obtain reservoir states. A microcontroller (Arduino UNO) was used to implement the writing (applying the masking inputs) and reading (obtaining the reservoir states) of the device through a serial port with a baud rate of 115,200 s^{-1}. The output matrix W_{OUT} is obtained through one-step linear regression with the target output. Speech signals are collected using the PC microphone. The individuals stand about 1 m away from the microphone and speak. The collected speech signals include cancel, confirm, up and down, with a duration of 1.0 s. In the recognition process, the collected inputs undergo feature extraction and masking in MATLAB and are inputted into the device for nonlinear output, which is then multiplied by W_{OUT}. The final recognition result is determined according to the winner-take-all principle.

In vivo evaluation of the HIRE

All animal experiments were approved by the institutional ethical committee of Jinling Hospital (ID no. 2023JLHGZRDWLS-00048). Female Sprague-Dawley rats (outbred stock; age, 8 weeks; body weight, 200–300 g), ordered from Jiangsu Huachuang XinNuo Biotechnology, were used to evaluate the performance of the HIRE after implantation. HIRE devices to be sterilized were placed into a class II microbiological safety cabinet (BioMAT2) and under ultraviolet light at a wavelength of 254 nm for 15 min. No statistical sample size calculation was performed. As this study was designed as a proof-of-concept to validate the in vivo technical feasibility and signal processing capability of the implanted HIRE device, rather than to evaluate biological variations, a representative sample size (n = 2) was chosen.

For subcutaneous implantation in rats, a full-thickness cutaneous wound with a diameter of approximately 1 cm was created on the dorsal area of the anaesthetized rat. Subsequently, the HIRE was placed subcutaneously into the rat through trauma. Following the wound's suturing, the in vivo performance of the HIRE-based network was tested via a speech-recognition task.

For neural stimulation in rats, the animals were anaesthetized with isoflurane (2–3% in oxygen) for induction and maintained in an anaesthetized state with 10% chloral hydrate throughout the procedure. The hair on the posterior thigh was shaved and the skin was disinfected with 75% ethanol. A longitudinal incision (~1.5 cm) was made along the lateral aspect of the thigh to expose the biceps femoris muscle. The HIRE was carefully implanted near the target muscle within the fascial plane, ensuring intimate contact with the surrounding tissue microenvironment. For sciatic nerve stimulation, the sciatic nerve was gently exposed through careful blunt dissection, avoiding damage to surrounding blood vessels. Custom-made bipolar hook electrodes (3 mm spacing) were positioned around the exposed sciatic nerve. The HIRE-based network was programmed to deliver electrical stimulation consisting of 100 biphasic pulses at a 67% duty cycle and 5 Hz frequency, with a pulse duration of 0.1 ms and amplitude of 0–5 V, following voice command recognition. Motor responses were monitored by observing hind-limb movement and locomotor behaviour. Muscle surface pH was immediately measured using a pen-type pH meter (AZ8695, AZ Instrument) with a pH measurement range of 2.0–12.0 (accuracy, ±0.1), pH resolution of 0.01 and temperature range of 0–80 °C (temperature

accuracy, ±0.5 °C). The pH measurements were taken at three different points on the muscle surface near the stimulation site, and the average value was recorded. After stimulation testing, the incision was sutured in layers using 4-0 absorbable sutures for muscle fascia and 4-0 non-absorbable sutures for skin closure.

The rats were housed individually with access to food and water in an animal room and euthanized by inhaling excessive isoflurane 9 days after the implantation. Tissues from the heart, liver, spleen, lung, kidney and intestine were harvested and immersed in a 10% formalin solution. The organs were subsequently embedded in paraffin, sectioned and stained with hematoxylin and eosin (H&E). Histological sections were observed using an optical microscope (IX71; Olympus). The pathologist was blinded to both the identity and analytical results of the pathology slides.

Reporting summary

Further information on research design is available in the Nature Portfolio Reporting Summary linked to this article.

Data availability

All data supporting the findings of this study are available in the paper and its Supplementary Information. Other raw data are available from the corresponding authors upon request. Source data are available via figshare at https://doi.org/10.6084/m9.figshare.31153141 (ref. 56).

Code availability

MATLAB codes for data processing and algorithm implementation have been deposited at GitHub at https://github.com/ONEGroup-nju/Code-for-iontronic-reservoir.git.

References

56. Mengjiao, P. Source data. *figshare* https://doi.org/10.6084/m9.figshare.31153141 (2026).

Acknowledgements

This work was supported by the National Key Research and Development Program of China (grant nos 2023YFE0208600 to C.W., 2021YFA1202600 to C.W., 2022YFA1203802 to Y. Li and 2021YFA0715600 to Y. Li), the National Natural Science Foundation of China (grant nos 62174082 to C.W., 92364106 to C.W., 92364204 to C.W., 82302321 to L.L., 62374081 to Y. Li and T2322010 to B.X.) and the Nanjing Municipal Science and Technology Bureau (grant nos 202305001 and 202205020 to C.W.). We thank the Leading Innovation and Entrepreneurship Team of Zhejiang Province, Ministry of Education Engineering Research Center for Optoelectronic Materials and Chip Technology and Nanjing University International Collaboration Initiative for support.

Author contributions

W.L. and M.P. conceived the initial idea and organized the research frame. M.P., T.G. and H.L. contributed to sample preparation and device fabrication. M.P. performed the simulations and hardware measurements and analysed the results. L.L., Z.T. and M.P. performed the implantation experiments and analysed the results. H.C. collected speech signals. X.L. implemented the GIST algorithm. K.S. and Q.D. performed the electrochemical impedance spectroscopy measurements. L.Q., B.P. and Q.X. assisted in the discussion on device physics. M.W., M.H. and Z.W. contributed to the mathematical fitting of the device models. M.P., C.W., T.G., W.L., Y. Luo and L.L. wrote and refined the paper. C.W., X.C., Q.W., B.X., Y.C., Y. Li and Y.S. supervised the project. All authors discussed the results and implications and commented on the manuscript at all stages.

Competing interests

The authors declare no competing interests.

Additional information

Extended data is available for this paper at https://doi.org/10.1038/s41563-026-02532-7.

Supplementary information The online version contains supplementary material available at https://doi.org/10.1038/s41563-026-02532-7.

Correspondence and requests for materials should be addressed to Yun Li, Bin Xue, Yi Shi, Qing Wan, Xiaodong Chen or Changjin Wan.

Peer review information *Nature Materials* thanks Kyung Min Kim, Tae-Woo Lee and Yoeri van de Burgt for their contribution to the peer review of this work.

https://doi.org/10.1038/s41563-026-02532-7

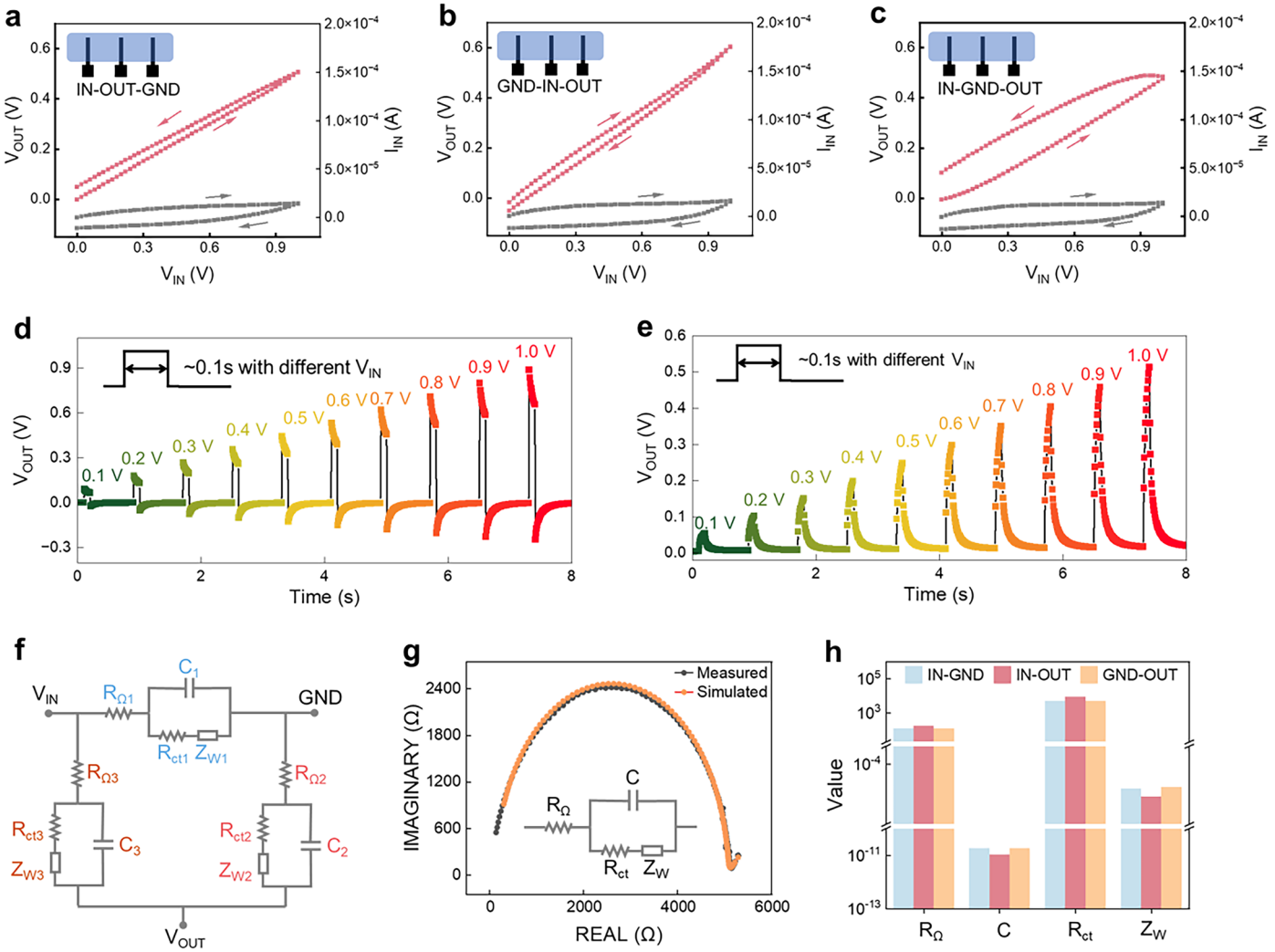

Extended Data Fig. 1 | Electrical characterization and impedance analysis of the device. a-c, V_{OUT}-V_{IN} hysteresis curves (red squares) and input current (black squares) characteristics for different electrode sequences. Output responses to electrical pulses (0.1 s duration) with varying input amplitudes for different electrode configurations: **d**, V_{OUT} positioned near V_{IN} electrode. **e**, V_{OUT} positioned near the GND electrode. Impedance analysis and model fitting of the HIRE device. **f**, Schematic diagram of the device equivalent model. **g**, Impedance fitting with the fitting model shown in the inset. **h**, Statistical analysis of parameters from the fitting results.

https://doi.org/10.1038/s41563-026-02532-7

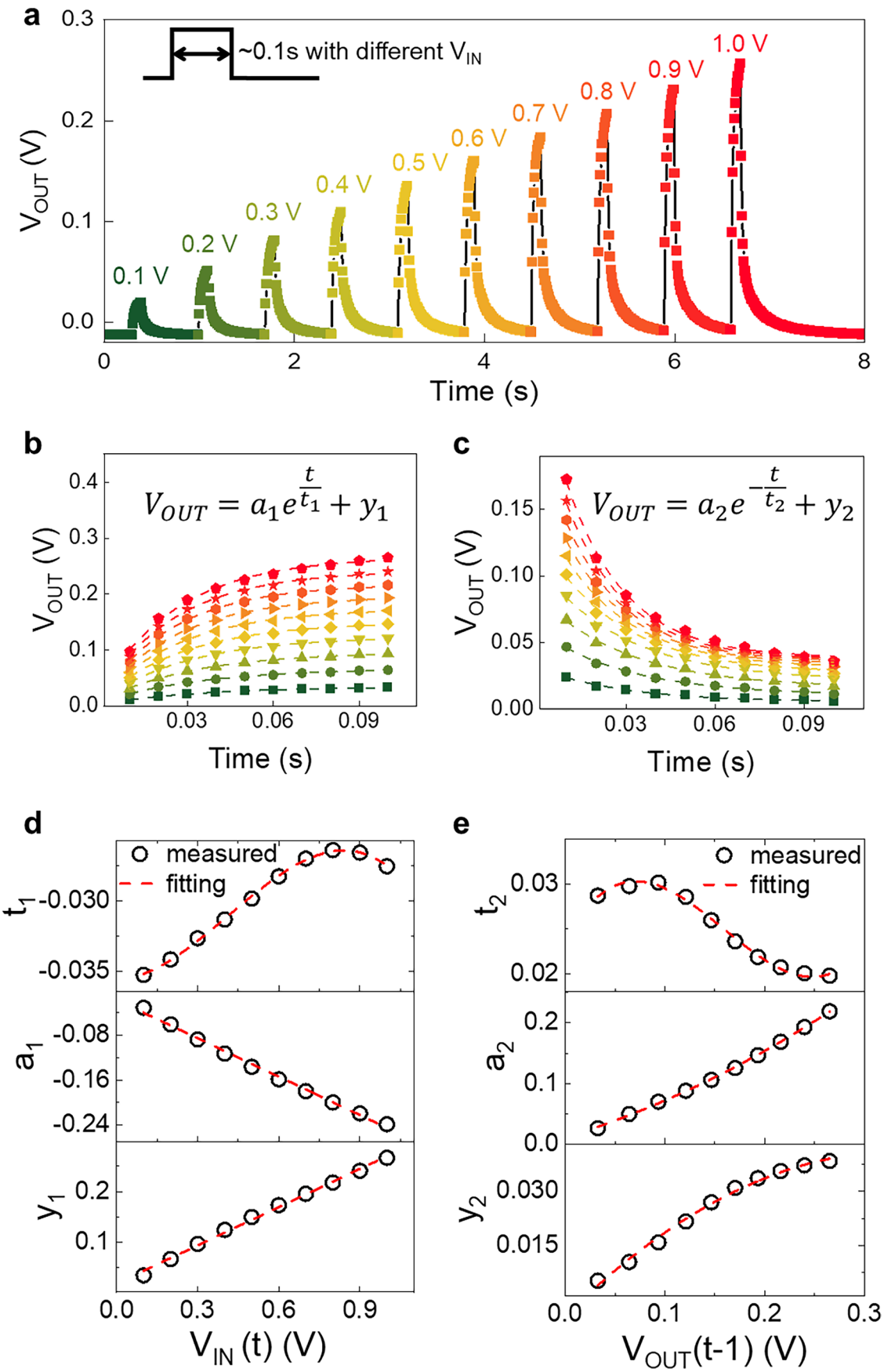

Extended Data Fig. 2 | Characterization and modelling of HIREs. a, Output results triggered by electrical pulses (0.1 s) with different amplitudes of inputs. The extracted measurements (symbols) for the **b**, increasing processes and **c**, decreasing processes. The corresponding dashed lines are the fitting results. **d**, Fitting parameters as a function of current input voltage V_{IN}(t) in the increasing processes. **e**, Fitting parameters as a function of the last state output voltage V_{OUT}(t-1) in the decreasing processes.

https://doi.org/10.1038/s41563-026-02532-7

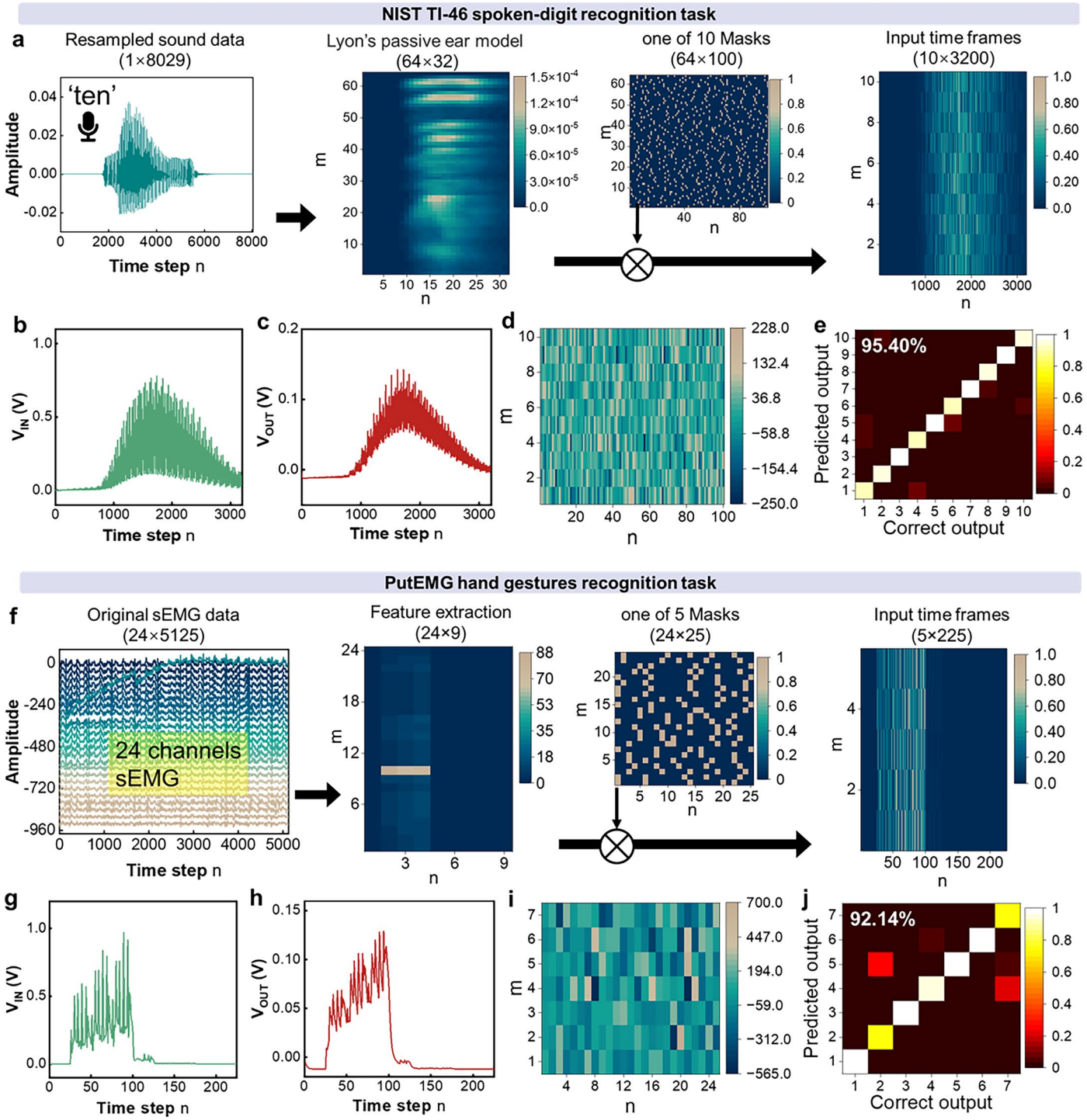

Extended Data Fig. 3 | NIST TI-46 spoken-digit and PutEMG hand gestures recognition task. a, Preprocessing of the raw signal data by feature extraction and masking, then converting it to the input voltage of the device. **b**, One of the input time frames to be applied to devices and **c**, the corresponding outputs of the HIRE. **d**, Output weight matrix. **e**, Recognition results (confusion matrix) for ten voices. The recognition accuracy is 95.40%. **f**, Preprocessing of the raw signal data by feature extraction and masking, then converting it to the input voltage of the device. **g**, One of the input time frames to be applied to devices and **h**, the corresponding outputs of the HIRE. **i**, Output weight matrix. **j**, Recognition results (confusion matrix) for seven gestures. The recognition accuracy is 92.14%.

https://doi.org/10.1038/s41563-026-02532-7

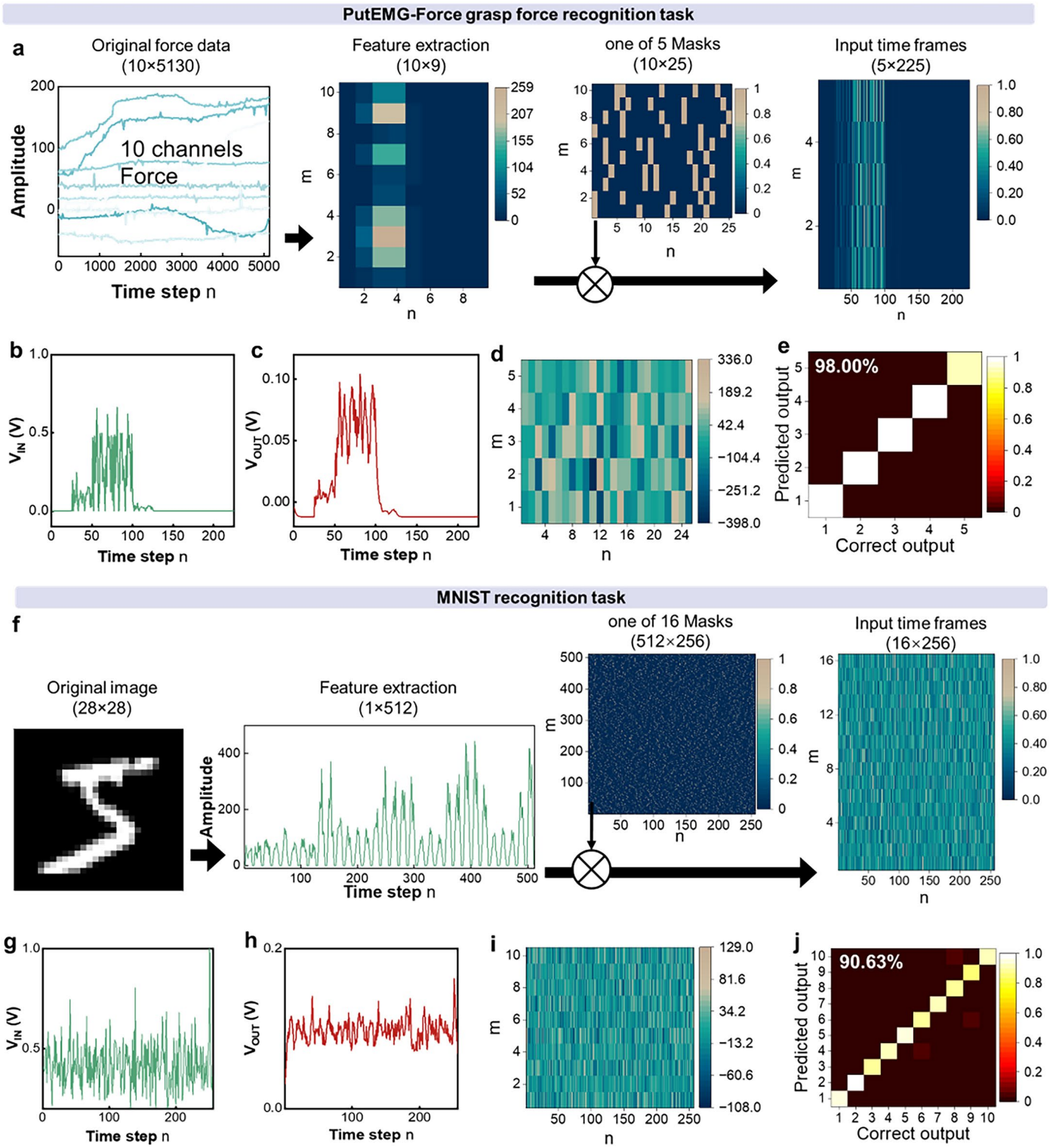

Extended Data Fig. 4 | PutEMG-Force grasp force and MNIST recognition task. **a**, Preprocessing of the raw signal data by feature extraction and masking, then converting it to the input voltage of the device. **b**, One of the input time frames to be applied to devices and **c**, the corresponding outputs of the HIRE. **d**, Output weight matrix. **e**, Recognition results (confusion matrix) for five types of grips. The recognition accuracy is 98.00%. **f**, Preprocessing of the raw signal data by feature extraction (Gabor convolution results) and masking, then converting it to the input voltage of the device. **g**, One of the input time frames to be applied to devices and **h**, the corresponding outputs of the HIRE. **i**, Output weight matrix. **j**, Recognition results (confusion matrix) for images of ten numbers. The recognition accuracy is 90.63%.

https://doi.org/10.1038/s41563-026-02532-7

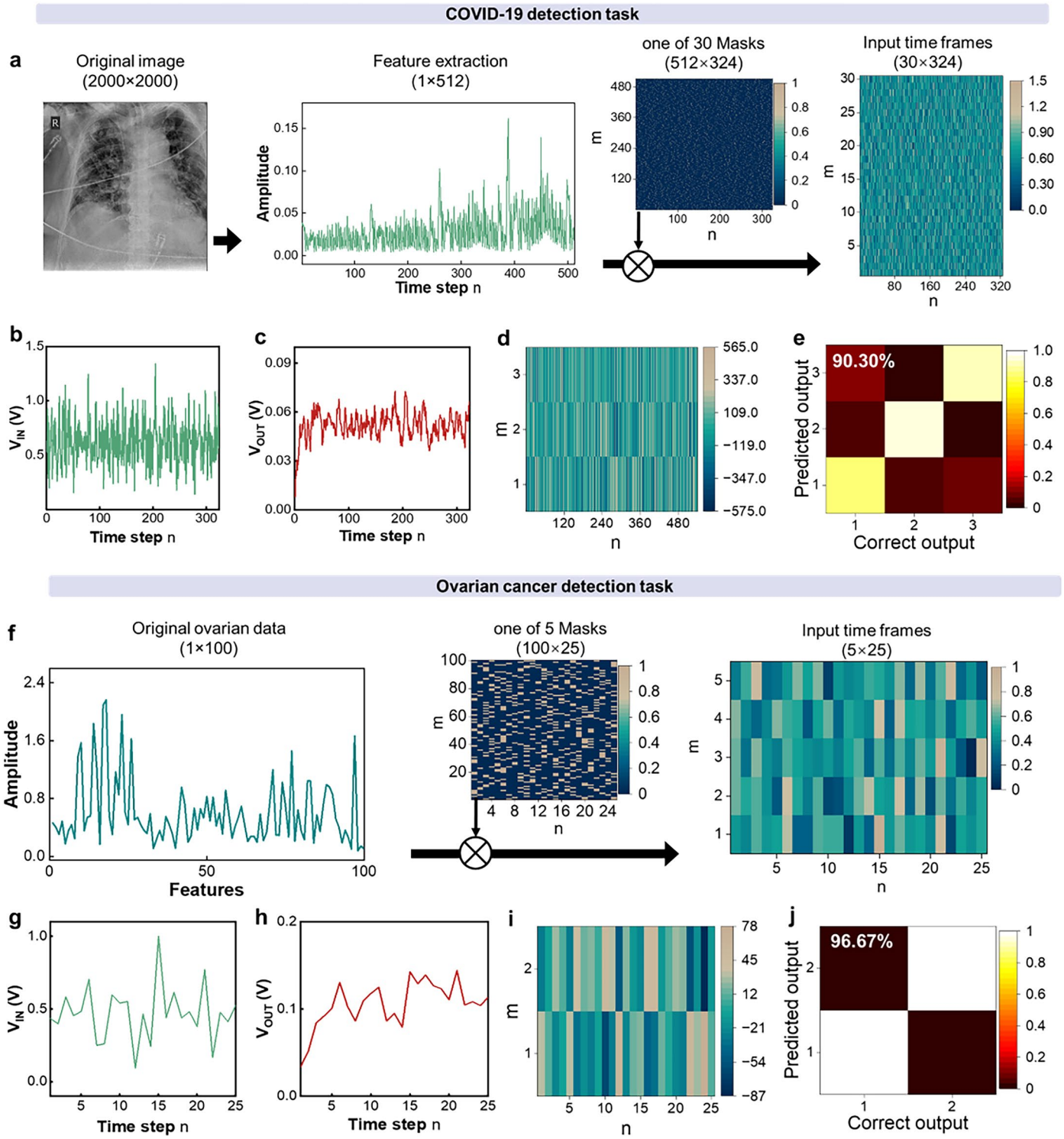

Extended Data Fig. 5 | COVID-19 and ovarian cancer detection task. **a**, Preprocessing of the raw signal data by feature extraction (Gabor convolution results) and masking, then converting it to the input voltage of the device. **b**, One of the input time frames to be applied to devices and **c**, the corresponding outputs of the HIRE. **d** Output weight matrix**. e**, Recognition results (confusion matrix) for three cases. The recognition accuracy is 90.30%. **f**, Preprocessing of the raw signal data by masking, then converting it to the input voltage of the device. **g**, One of the input time frames to be applied to devices and **h**, the corresponding outputs of the HIRE. **i**, Output weight matrix. **j**, Recognition results (confusion matrix) for diseased and non-diseased patients. The recognition accuracy is 96.67%.

https://doi.org/10.1038/s41563-026-02532-7

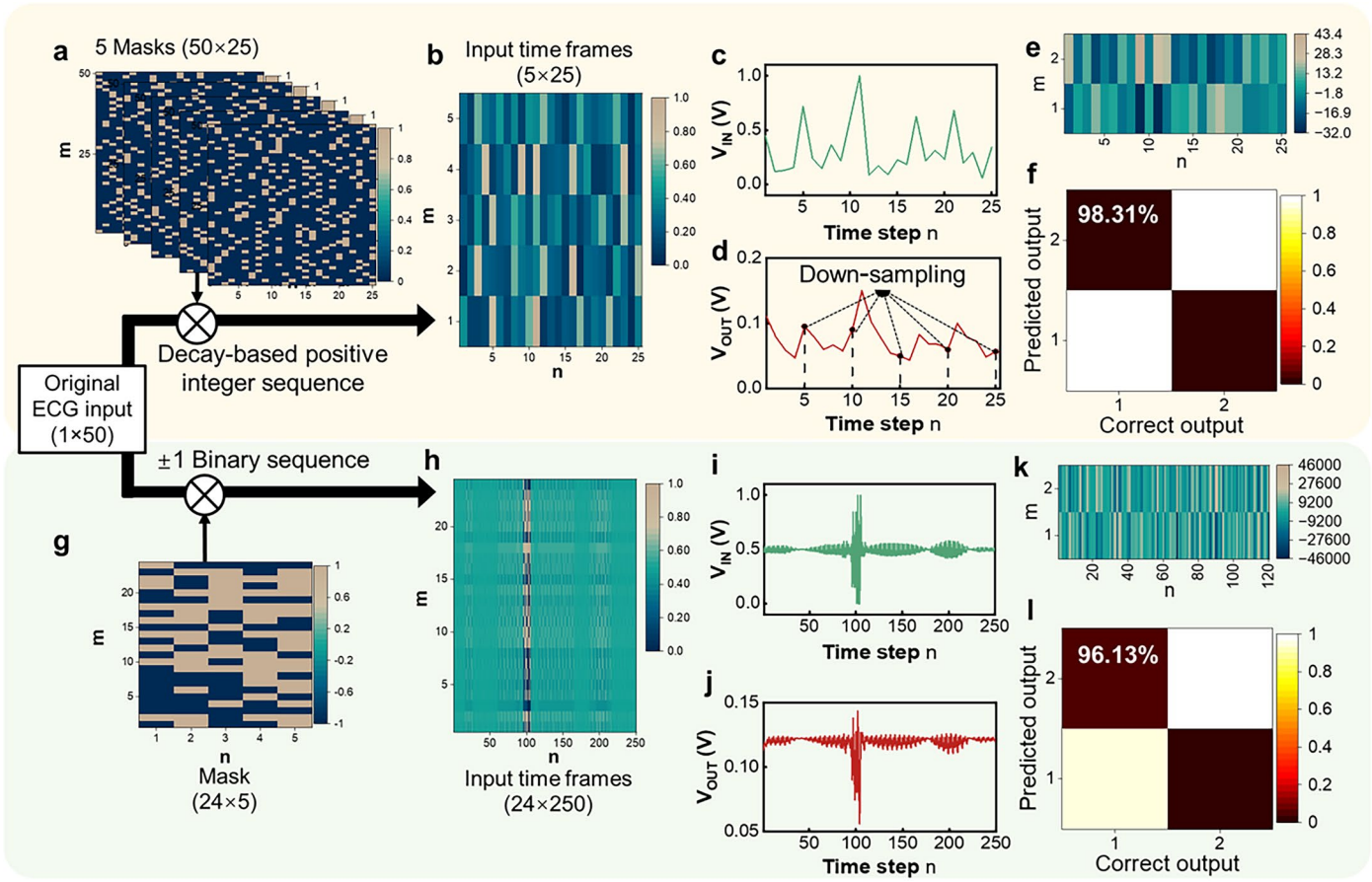

Extended Data Fig. 6 | ECG diagnosis task. a, Different mask matrices applied to 5 devices based on decay-based positive integer sequences. **b**, Input sequences after mask matrix processing. **c**, One of the input time frames applied to devices and **d**, the corresponding outputs of the HIRE. **e**, Output weight matrix. **f**, Recognition results (confusion matrix) for healthy and arrhythmic heartbeats with recognition accuracy of 98.31%. **g**, Different mask matrices applied to 24 devices based on ±1 binary sequences. **h**, Input sequences after mask matrix processing. **i**, One of the input time frames applied to devices and **j**, the corresponding outputs of the HIRE. **k**, Output weight matrix. **l**, Recognition results (confusion matrix) for healthy and arrhythmic heartbeats with recognition accuracy of 96.13%. The proposed method employs a 3D decay-based positive integer sequence input mask, where 3D refers to the dimensionality of the mask matrix. This approach generates more complex and separable reservoir states, thereby enabling high-accuracy linear regression while maintaining low computational complexity.

https://doi.org/10.1038/s41563-026-02532-7

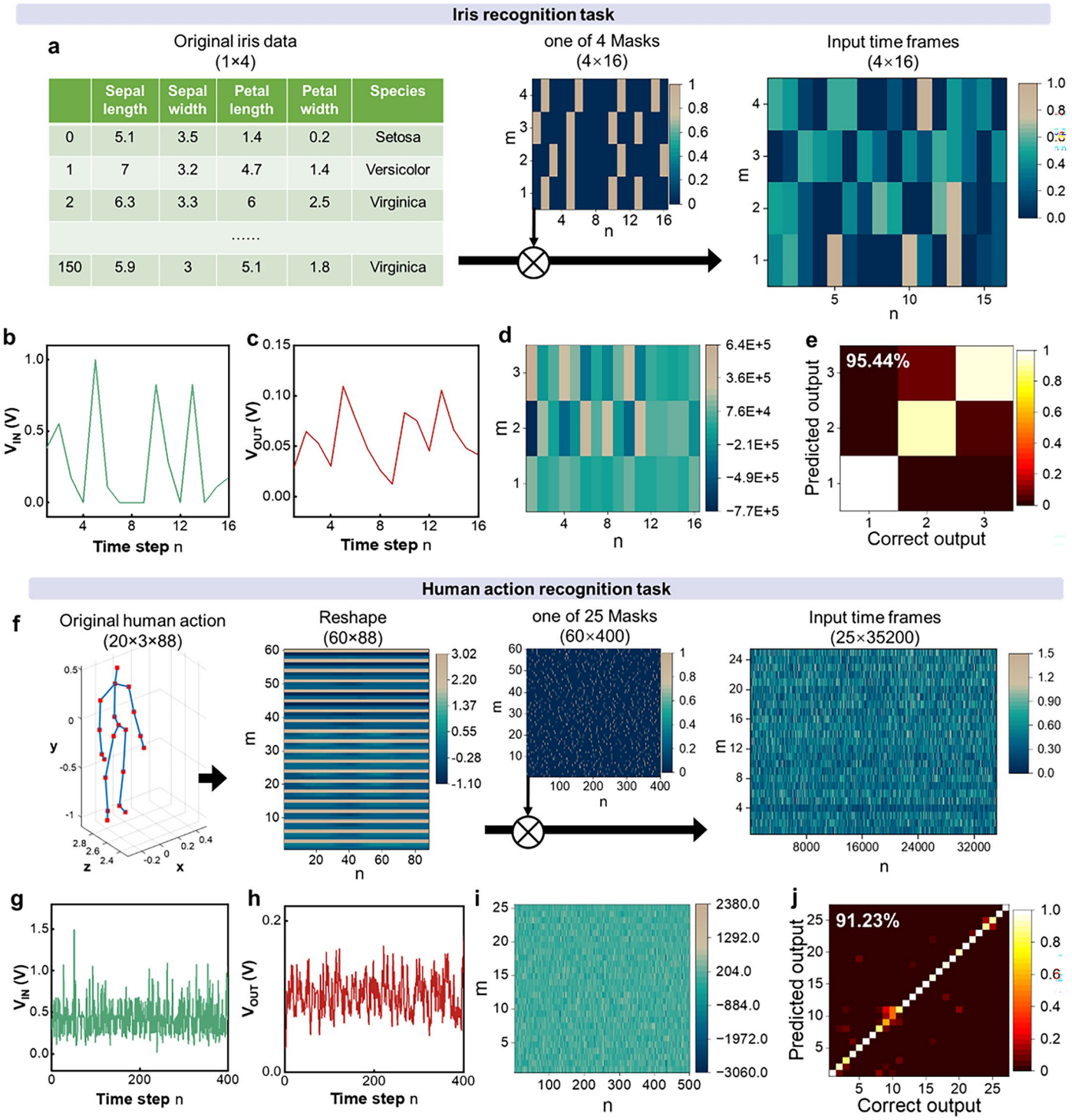

	Sepal length	Sepal width	Petal length	Petal width	Species
0	5.1	3.5	1.4	0.2	Setosa
1	7	3.2	4.7	1.4	Versicolor
2	6.3	3.3	6	2.5	Virginica
			.....		
150	5.9	3	5.1	1.8	Virginica

Extended Data Fig. 7 | Iris and human action recognition task. a, Preprocessing of the raw signal data by masking, then converting it to the input voltage of the device. **b**, One of the input time frames to be applied to devices and **c**, the corresponding outputs of the HIRE. **d**, Output weight matrix. **e**, Recognition results (confusion matrix) for three species of iris flowers. The recognition accuracy is 95.44%. **f**, Preprocessing of the raw signal data by masking, then converting it to the input voltage of the device. **g**, One of the input time frames to be applied to devices and **h**, the corresponding outputs of the HIRE. The first 100 points were selected for the waveform to be visible. **i**, Output weight matrix. **j**, Recognition results (confusion matrix) for 27 human actions. The recognition accuracy is 94.20%.

https://doi.org/10.1038/s41563-026-02532-7

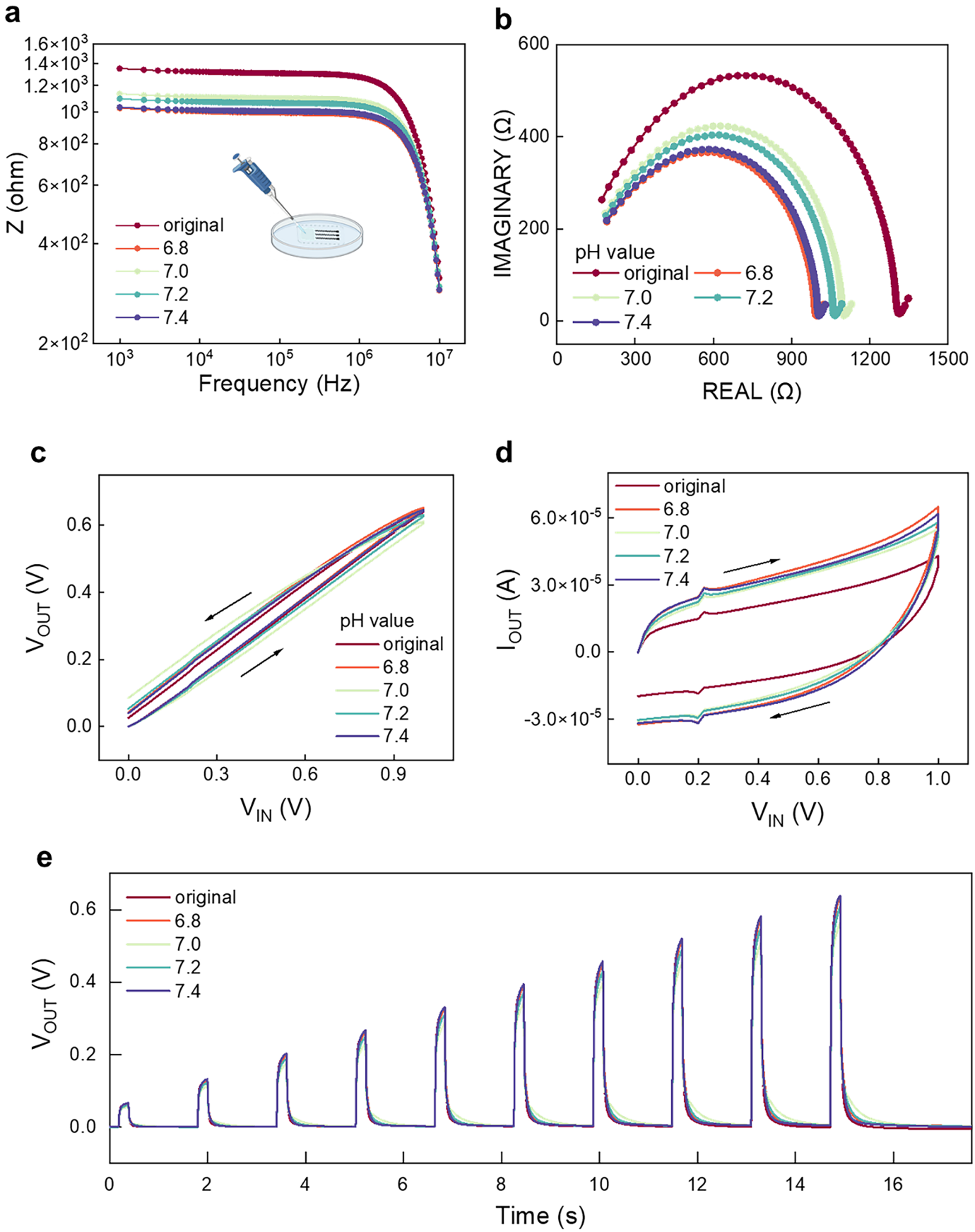

Extended Data Fig. 8 | pH-dependent device characteristics. a, Impedance-frequency relationship of original samples under different pH environments. **b**, Nyquist plots. **c**, V_{OUT}-V_{IN} hysteresis curves. **d**, I_{IN}–V_{IN} characteristics. **e**, Output responses triggered by electrical pulses (0.2 s duration) with input amplitudes ranging from 0.1 V to 1 V. Illustration in **a** created in BioRender. Pei, M. https://BioRender.com/s5u94ya (2026).

https://doi.org/10.1038/s41563-026-02532-7

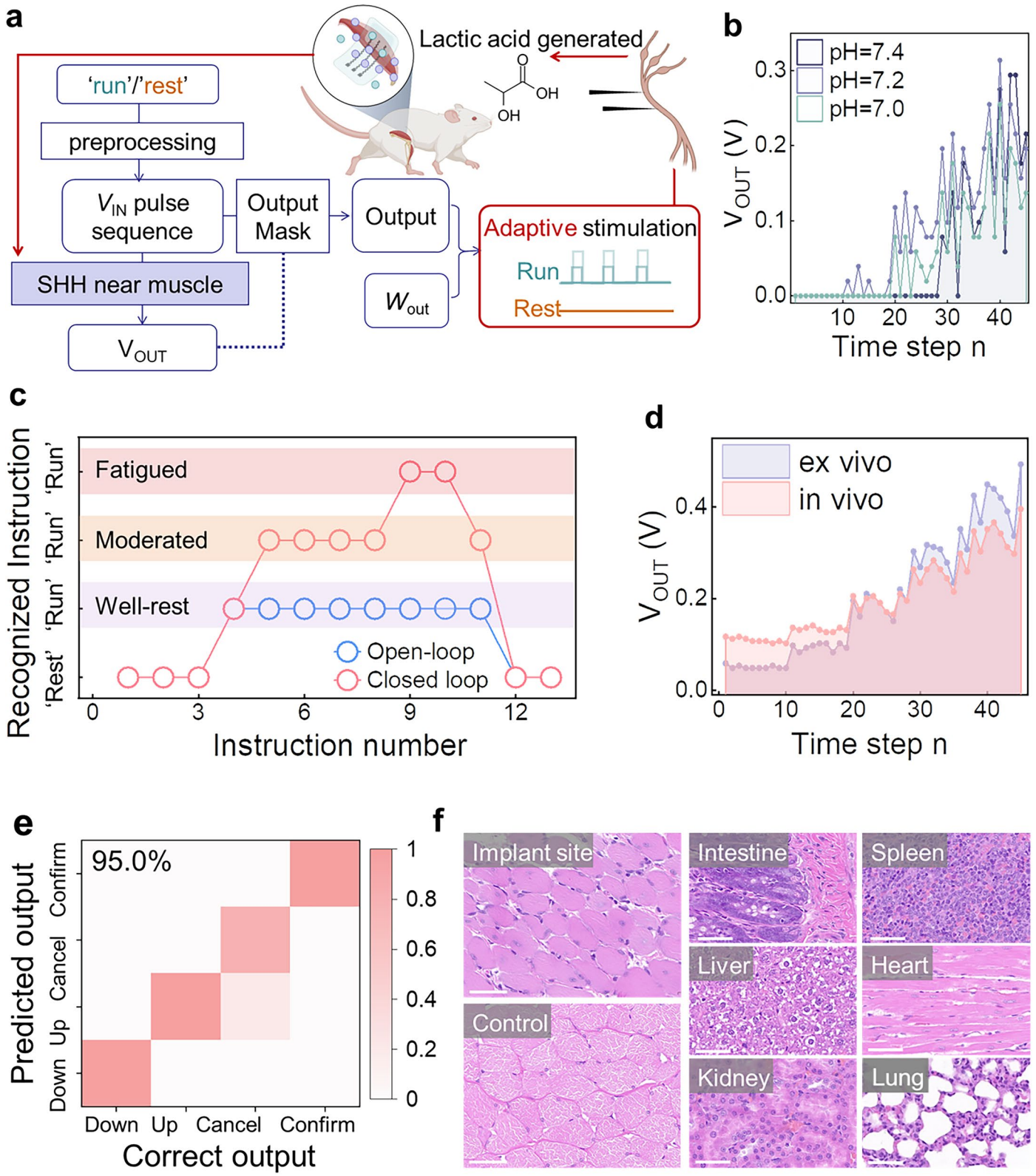

Extended Data Fig. 9 | Closed-loop neural stimulation control and biocompatibility assessment. a, Process flow for controlling rat sciatic nerve stimulation using voice commands through pH-adaptive SHH-based bio-hybrid neuromorphic systems. **b**, Responses of the hydrogel reservoir to identical time series inputs under different pH conditions during voice command ('Run') recognition tasks. **c**, Recognition results under identical input command sequences for open-loop and closed-loop systems. **d**, The responses of the hydrogel reservoir to the same time series inputs before (green) and after (yellow) implantation. **e**, Confusion matrix for the spoken recognition task. **f**, H&E-stained sections (scale bar: 50 μm) of major organs from the sacrificed rat 9 days after implantation. Illustration in **a** created in BioRender. Pei, M. https://BioRender.com/io6ouei (2026).

https://doi.org/10.1038/s41563-026-02532-7

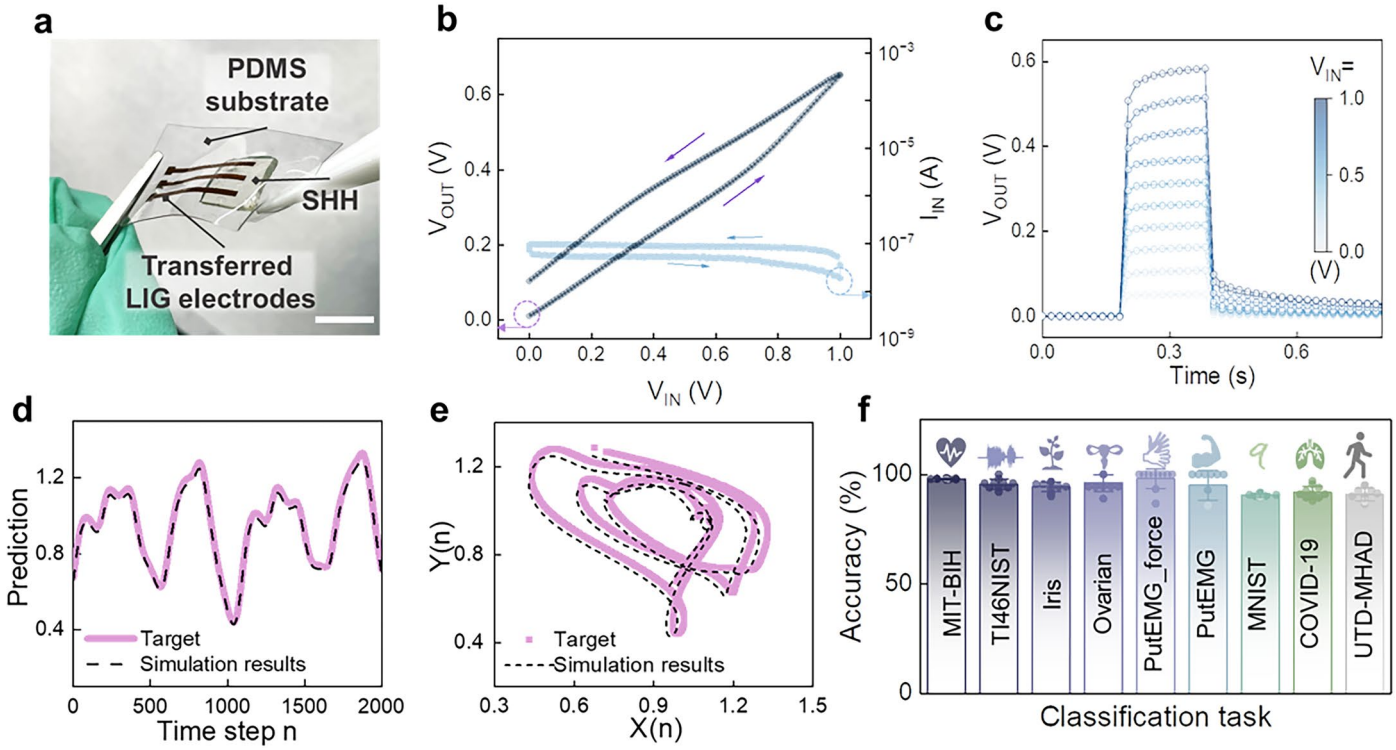

Extended Data Fig. 10 | Characterization of devices and demonstration of computing tasks using fully biocompatible devices. a, Schematic illustration of PDMS-based soft device. **b**, V_{OUT}-V_{IN} hysteresis loops and corresponding input current. **c**, Response to electrical pulse stimulation with different amplitudes ranging from 0.1 to 1 V and pulse width of 0.2 s. **d**, Forecasting results of the Mackey–Glass time series, where the pink line represents the actual data to be estimated and the black dotted line represents the predicted output based on the device model. **e**, 2-D display of the predicted results. **f**, Classification accuracy for nine different intelligent tasks using standard datasets. Data are presented as mean values ± SD with n = 10 (10-fold cross-validation).

nature portfolio

Corresponding author(s): Xiaodong Chen

Last updated by author(s): Jan 5, 2026

Reporting Summary

Nature Portfolio wishes to improve the reproducibility of the work that we publish. This form provides structure for consistency and transparency in reporting. For further information on Nature Portfolio policies, see our Editorial Policies and the Editorial Policy Checklist.

Statistics

For all statistical analyses, confirm that the following items are present in the figure legend, table legend, main text, or Methods section.

n/a	Confirmed	
☐	☒	The exact sample size (*n*) for each experimental group/condition, given as a discrete number and unit of measurement
☐	☒	A statement on whether measurements were taken from distinct samples or whether the same sample was measured repeatedly
☒	☐	The statistical test(s) used AND whether they are one- or two-sided *Only common tests should be described solely by name; describe more complex techniques in the Methods section.*
☐	☒	A description of all covariates tested
☐	☒	A description of any assumptions or corrections, such as tests of normality and adjustment for multiple comparisons
☐	☒	A full description of the statistical parameters including central tendency (e.g. means) or other basic estimates (e.g. regression coefficient) AND variation (e.g. standard deviation) or associated estimates of uncertainty (e.g. confidence intervals)
☒	☐	For null hypothesis testing, the test statistic (e.g. *F*, *t*, *r*) with confidence intervals, effect sizes, degrees of freedom and *P* value noted *Give P values as exact values whenever suitable.*
☒	☐	For Bayesian analysis, information on the choice of priors and Markov chain Monte Carlo settings
☒	☐	For hierarchical and complex designs, identification of the appropriate level for tests and full reporting of outcomes
☒	☐	Estimates of effect sizes (e.g. Cohen's *d*, Pearson's *r*), indicating how they were calculated

Our web collection on statistics for biologists contains articles on many of the points above.

Software and code

Policy information about availability of computer code

Data collection	Data collection are listed in Methods. All softwares used in this study for data collection are either commercially available or open source.
Data analysis	All software used in this study for data analysis are either commercially available or open source. For example, CaseViewer 2.4, Arduino IDE 2.3.4, Origin2016, and MATLAB R2022b.

For manuscripts utilizing custom algorithms or software that are central to the research but not yet described in published literature, software must be made available to editors and reviewers. We strongly encourage code deposition in a community repository (e.g. GitHub). See the Nature Portfolio guidelines for submitting code & software for further information.

Data

Policy information about availability of data

All manuscripts must include a data availability statement. This statement should provide the following information, where applicable:

- Accession codes, unique identifiers, or web links for publicly available datasets
- A description of any restrictions on data availability
- For clinical datasets or third party data, please ensure that the statement adheres to our policy

The author declares that all data that support the findings of the study are available within the paper and the Supplementary Information.

Human research participants

Policy information about studies involving human research participants and Sex and Gender in Research.

Reporting on sex and gender	The study did not involve human participants.
Population characteristics	N. A.
Recruitment	N. A.
Ethics oversight	N. A.

Note that full information on the approval of the study protocol must also be provided in the manuscript.

Field-specific reporting

Please select the one below that is the best fit for your research. If you are not sure, read the appropriate sections before making your selection.

☒ Life sciences ☐ Behavioural & social sciences ☐ Ecological, evolutionary & environmental sciences

For a reference copy of the document with all sections, see nature.com/documents/nr-reporting-summary-flat.pdf

Life sciences study design

All studies must disclose on these points even when the disclosure is negative.

Sample size	No sample size calculations were performed. Sample size was determined by the number of biological and technical replicates to confirm that the effect was real. The number of biological replicates was 3-6 with several technical replicates in each sample.
Data exclusions	No data was excluded from the analysis.
Replication	All experiment findings, including electrochemical testing, electrical characterization, mechanical characterization, SEM images, cell-related measurements, and living animal measurements were reliably reproduced for 3-6 times.
Randomization	In the reported experiments, each group consisted of identically engineered samples. The work does not involve participant groups. Therefore, randomization was not relevant the study.
Blinding	Blinding was not relevant to our experiments as the results of device capability, cell response and the movement of mouse leg were quantitative and did not involve subjective judgement or interpretation.

Reporting for specific materials, systems and methods

We require information from authors about some types of materials, experimental systems and methods used in many studies. Here, indicate whether each material, system or method listed is relevant to your study. If you are not sure if a list item applies to your research, read the appropriate section before selecting a response.

Materials & experimental systems

n/a	Involved in the study
☒	☐ Antibodies
☒	☐ Eukaryotic cell lines
☒	☐ Palaeontology and archaeology
☐	☒ Animals and other organisms
☒	☐ Clinical data
☒	☐ Dual use research of concern

Methods

n/a	Involved in the study
☒	☐ ChIP-seq
☒	☐ Flow cytometry
☒	☐ MRI-based neuroimaging

Animals and other research organisms

Policy information about studies involving animals; ARRIVE guidelines recommended for reporting animal research, and Sex and Gender in Research

Laboratory animals	Adult rats (Sprague Dawley rats, Anuokang Biotech) were used in the study. Rat are housing at Jinling Hospital, Affiliated Hospital of Medical School, Nanjing University at temperature of 22 oC, 40%-60% humidity.
Wild animals	The study did not involve wild animals.
Reporting on sex	Sex based analysis was not performed in the study because this study did not involve sex-related variables.
Field-collected samples	The study did not involve samples collected from field.
Ethics oversight	Animal experiments were approved by Jinling Hospital, Affiliated Hospital of Medical School, Nanjing University (NO. 2023JLHGZRDWLS-00048).

Note that full information on the approval of the study protocol must also be provided in the manuscript.